

LETFULLINA, ALLA, Ph.D. Investigation of Plastic Crystal and Metal-Organic Framework-Based Solid-State Electrolytes. (2021)
Directed by Dr. Hemali Rathnavake. 74 pp.

The all-solid-state battery is hailed as the next generation of energy storage. It has the potential to drastically improve the safety, energy density, and cost of the battery. Therefore, there have been many avenues developed to achieve a solid-state electrolyte (SSE). This project focuses on the two least investigated approaches of SSE advancement. The first approach utilizes a plastic crystal to improve the ionic conductivity of a solid polymer electrolyte (SPE), while the latter explores the possibility of employing a lithium-based metal-organic framework (MOF) as a solid-state electrolyte. Although there is much research performed on various plastic crystal electrolytes, their ion conduction mechanism remains a controversial topic. Similarly, MOFs are a novel class of materials, and their functionality within the lithium-ion battery needs to be further examined. This work studies the synthesis, thermal, electrochemical, and optical properties of the plastic crystal and MOF electrolytes, with an emphasis on their ion conduction mechanism.

INVESTIGATION OF PLASTIC CRYSTAL AND METAL ORGANIC
FRAMEWORK-BASED SOLID-STATE ELECTROLYTES

by

Alla Letfullina

A Dissertation Submitted to
the Faculty of The Graduate School at
The University of North Carolina at Greensboro
in Partial Fulfillment
of the Requirements for the Degree
Doctor of Philosophy

Greensboro
2021

Approved by

Committee Chair

Dedicated to my family (Tatiana Letfullina, Renat Letfullin, and Mary Letfullin), my friends, and my wonderful boyfriend, Dr. Taylor Mabe, and his family. Thank you for your support.

APPROVAL PAGE

This dissertation, written by ALLA LETFULLINA, has been approved by the following committee of the Faculty of The Graduate School at The University of North Carolina at Greensboro.

Committee Chair _____

Committee Members _____

Date of Acceptance by Committee

Date of Final Oral Examination

ACKNOWLEDGMENTS

I would like to acknowledge my wonderful advisors, Dr. Rathnayake and Dr. LaJeunesse, and my exceptional committee, Dr. Ignatova and Dr. Herr, for their support.

TABLE OF CONTENTS

	Page
LIST OF TABLES	vii
LIST OF FIGURES	viii
 CHAPTER	
I. INTRODUCTION	1
1.1 Energy Storage Demand	1
1.2 Fundamentals of Electrochemical Energy Storage	2
1.3 LIB Challenges	5
1.4 The Solid-State Battery	6
1.5 Plastic Crystal Electrolytes	8
1.6 Metal-Organic Frameworks	11
1.7 MOF Use in Lithium-Ion Batteries	11
1.8 General Goal of Research	13
1.9 References	15
II. BACKGROUND	20
2.1 Ionic Conductivity Mechanism of SPES	20
2.2 Ionic Conductivity of MOFs	22
2.3 Ionic Conductivity Measurements	25
2.4 References	28
III. EXPERIMENTAL	30
3.1 Materials	30
3.2 Characterization	31
3.3 Experimental Procedures	33
IV. RESULTS AND DISCUSSION	40
4.1 LiPF ₆ /GN/PAN/EC Electrolyte System	40
4.1.1 Lithium-Ion Conduction Mechanism Within LiPF ₆ /GN/PAN/EC System	40
4.1.2 The Applicability of LiPF ₆ /GN/PAN/EC System	45
4.1.3 Concluding Remarks Regarding LiPF ₆ /GN/PAN/EC System	50

4.2 LiClO ₄ /GN/PAN System.....	52
4.2.1 Interaction Between Li ⁺ Ions and Glutaronitrile	52
4.2.2 Interaction Between Li ⁺ Ions and Glutaronitrile Within a Polymer.....	55
4.2.3 Concluding Remarks Regarding LiClO ₄ /GN/PAN System	60
4.3 Zn MOF as Ion Conductors	61
4.3.1 Zn MOF Ionic Conductivity	61
4.3.2 Improving Ionic Conductivity of Zn MOF Using Electrolytic Solutions	63
5.3 Conclusion	68
5.4 References	70

LIST OF TABLES

	Page
Table 1.1. Assessment of Different Solid Electrolyte Properties	7
Table 4.1. Calculated Ionic Conductivities of LiClO ₄ /PAN (No GN) and LiClO ₄ /GN/PAN (With GN) Systems at 24°C	58
Table 4.2. Calculated Electrical Conductance Values of LiClO ₄ /PAN and LiClO ₄ /GN/PAN Systems	60
Table 4.3. Ionic conductivity results of Zn MOF pellet with added 10wtl% LiClO ₄ /THF, 10wt% LiClO ₄ /DMF, and 6wt% LiClO ₄ /GN	65

LIST OF FIGURES

	Page
Figure 1.1. Projection of the Electric Vehicle Market Sales	2
Figure 1.2. Lithium-Ion Battery Schematic.....	4
Figure 2.1. a) Li ⁺ Transport Within a Polymer; 1 b) VFT (Dotted Line) and Arrhenius (Solid Line) Ion Conductivity Behavior	21
Figure 2.2. A Schematic of the Grotthuss Mechanism.....	23
Figure 2.3. a) Typical Shape of a Nyquist Plot; b) Model Circuit Used to Fit the Nyquist Plot Shown in a)	26
Figure 4.1 a) Photograph of Alumina-SPE; b) Photographs of a Flexed Alumina-SPE; c) SEM Image of Bare-SPE at 5,000X; d) SEM Image of Alumina-SPE at 5,000X; e) SEM Image of Bare-SPE at 50,000X; f) SEM Image of Alumina-SPE at 50,000X	41
Figure 4.2. a) Nyquist Plots of Alumina-SPE; b) Temperature Dependence of Ionic Conductivity of Alumina-SPE.....	42
Figure 4.3. a) FTIR Results for LiPF ₆ -GN-EC, LiPF ₆ -PAN-EC, Bare-SPE and Alumina-SPE; b) Enlarged Peak at ~2240 cm ⁻¹ With the Sample Curves Overlapping to Emphasize Differences; c) Enlarged Peak at ~1770 cm ⁻¹ With the Sample Curves Overlapping to Emphasize Differences	43
Figure 4.4. a) LSV Results of SPE Membranes Compared to Liquid Electrolyte (1 M LiPF ₆ -EC-DEC) Soaked Polyethylene Separator; b) CV Result of Alumina-SPE Membrane; c) TGA Results of SPE Membranes Compared to Liquid Electrolyte (1 M LiPF ₆ -EC-DEC) Soaked Polyethylene Separator; d) Photographs of the SPE Membranes and Polyethylene Separator With and Without Liquid Electrolyte (1 M LiPF ₆ -EC-DEC) at 25°C (Top Row) and 150°C (Bottom Row)	46
Figure 4.5. a) Tensile Testing Results of the Bare and Alumina SPE; b) Potential Difference of an All Solid NMC622/Graphite Pouch Cell Made With Alumina-SPE Membrane; c) Demonstration of an All Solid State Pouch NMC622/Graphite Cell Assembled With the Alumina-	

	SPE as it Lights a Blue LED; d) Nail Penetration Test of the All Solid State Cell Depicted in b) and c) Which Results in Six Fully Penetrative Holes Which are Circled in Red; e) Demonstration of an All Solid State Pouch NMC622/Graphite Cell Assembled With the Alumina-SPE as it Retains >3.9 V After it Has Been Penetrated With a Drill	49
Figure 4.6.	a) Voltage Profile During the Formation Cycle of the NMC622/Graphite Pouch Cells Performed at 23°C Using a Current Rate of 0.1C; b) Capacity Retention Graphs of the NMC622/Graphite Coin Cells Conducted at 23°C Using a Current Rate of 0.3C, Which Results in a Current Density of 0.264 mA/cm ² ; c) Cycling of an All Solid State NMC622/Graphite Pouch Cell at 23°C Using a Current Rate of 0.3C Which Results in a Current Density of 0.268 mA/cm ² ; d) the All Solid State NMC622/Alumina-SPE/Graphite Pouch Cell Lighting a White LED (3.4V)	50
Figure 4.7.	FTIR Spectra of GN and the LiClO ₄ /GN System at 23°C	53
Figure 4.8.	FTIR Spectra of GN and the LiClO ₄ /GN System at 80°C	54
Figure 4.9.	FTIR Spectra of LiClO ₄ /PAN System at 23°C	55
Figure 4.10.	FTIR Spectra of GN and the LiClO ₄ /GN/PAN System at 23°C	56
Figure 4.11.	a) Nyquist Plots of the LiClO ₄ /PAN System at 24°C; b) Nyquist Plot of the LiClO ₄ /GN/PAN System at 24°C	57
Figure 4.12.	IV Plots of the LiClO ₄ /PAN and LiClO ₄ /GN/PAN Systems	59
Figure 4.13.	SEM Images of Zn MOF	62
Figure 4.14.	Nyquist Plots of Zn MOF Pellet With of a) 10 µL of Deionized Water at Measurement and After 20 Minutes, b) Various Amounts of 10wt% LiClO ₄ /DMF Solution, c) Various Amounts of 10wt% LiClO ₄ /TMF Solution and d) Various Amounts of 10 wt% LiClO ₄ /GN	63

CHAPTER I

INTRODUCTION

1.1 Energy Storage Demand

Our society has grown to be dependent on a reliable and continuous supply of electric power. In order to satisfy this demand, electric energy must not only be consistently generated but also stored. Furthermore, the alarming condition of our environment has created a much-needed push towards sustainable technologies. For example, air pollution in China contributes to 1.6 million deaths per year, according to a 2015 study performed by Rohde and Muller.¹ This has resulted in rapid advances in the energy harvesting industry and especially electric vehicles (EVs). Electric cars would not only dramatically improve the environment but will also increase road safety with the development of autonomous vehicles (AVs). AVs are closely related to EVs because for the vehicle to be truly autonomous, it must refuel itself, which would only be possible with a charging station. Currently, the auto manufacturers have invested \$150 billion in their plan to produce 13 million EVs annually by the year 2025.² A recent report on the growth of the EV market states that by the year 2040, EVs will account for 35% of all new car sales, as can be seen in Figure 1.1.³ The BMW Group already has delivered more than 100,000 electrified vehicles to customers worldwide in 2017.² Therefore, the global electrification of the auto market is no longer the dreams of the future, but a certain reality. However, the progress of the EV industry, as well as many other electronic

devices, is intimately tied to energy storage development. Therefore, this work focuses on methods to improve energy storage.

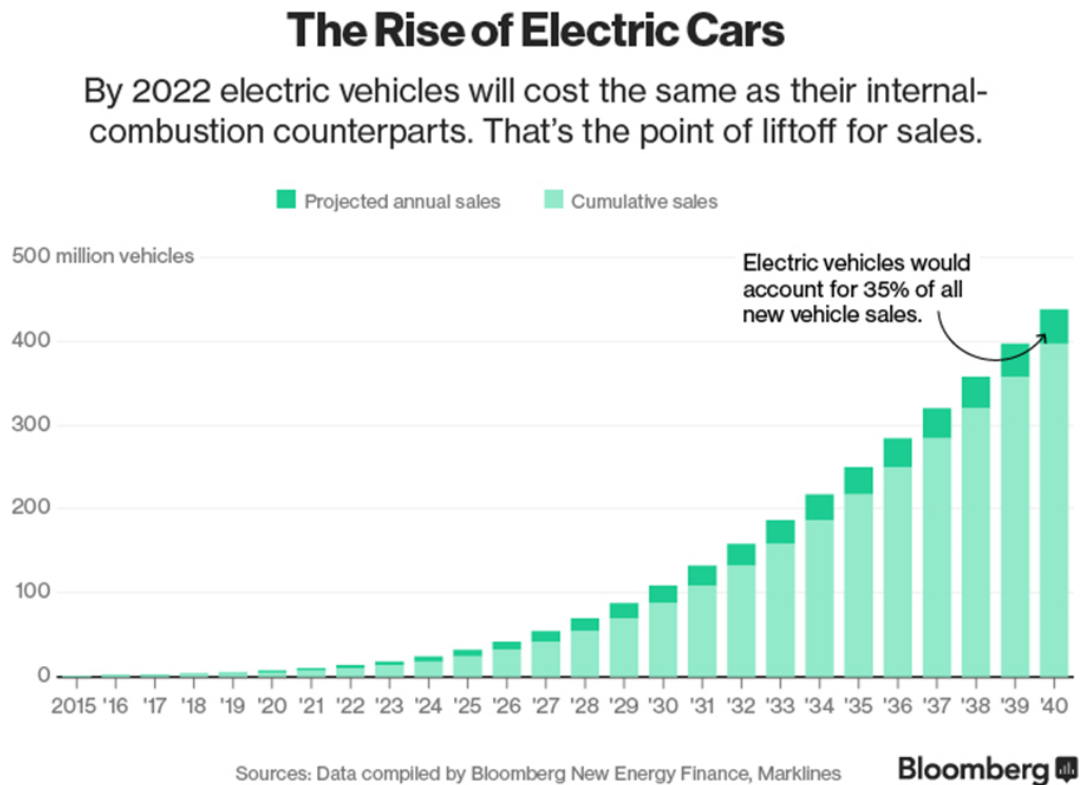


Figure 1.1. Projection of the Electric Vehicle Market Sales.³

1.2 Fundamentals of Electrochemical Energy Storage

The most common way to store electricity is via a battery.⁴ A battery is a device composed of one or more electrochemical cells, which derive electric energy from chemical reactions.⁴ Many types of batteries differ based on their chemical components. Batteries are divided into primary and secondary categories.⁴ The primary battery is a single-use device, which cannot be recharged.⁴ Primary batteries are used in remotes, toys, watches, etc. Secondary batteries are rechargeable and are used in cell phones,

laptops, and electric vehicles.⁴ Secondary batteries are utilized in a wider range of applications. Several chemistries permit a rechargeable battery: lead-acid, potassium ion, nickel-metal hydride, nickel-cadmium, and lithium ion.⁵⁻⁷ The lithium-ion battery (LIB) is the most prevalent due to its high energy density, negligible self-discharge, long life span, quick charging, and light weight.^{5,8} Therefore, the lithium-ion battery will be the focus of this project.

A lithium-ion battery consists of three main components: a positive electrode, a negative electrode, and an electrolyte, as shown in Figure 1.2.^{6,9} The positive electrode/cathode is the source of lithium ions, and its composition determines the amount of energy available within the battery.⁶ The negative electrode/anode accepts and hosts lithium ions during charging.⁶ The electrolyte transfers lithium ions between the electrodes.⁷ In a secondary battery, the reactions are not spontaneous, and an external force in the form of an electric field must be applied.^{4,9} During the charging process, the lithium in the cathode is oxidized to form a lithium ion, which travels via electrolyte to the anode where it is reduced.^{4,9} When a load is applied, the battery discharges, and the reverse of the process occurs.^{4,9} The electrons from the redox reactions travel via current collectors located on the outside of each electrode.^{4,9} The number of lithium ions participating in these reactions and the rate they are shuttled across the electrolyte determines how much current can be supplied by the battery, directly proportional to the battery's power.⁹ Despite many studies performed on the lithium-ion battery, the chemistry underlying its function is complex, intricate, and still unclear. More research

will be needed to resolve details in mechanisms and fully develop this energy storage device.

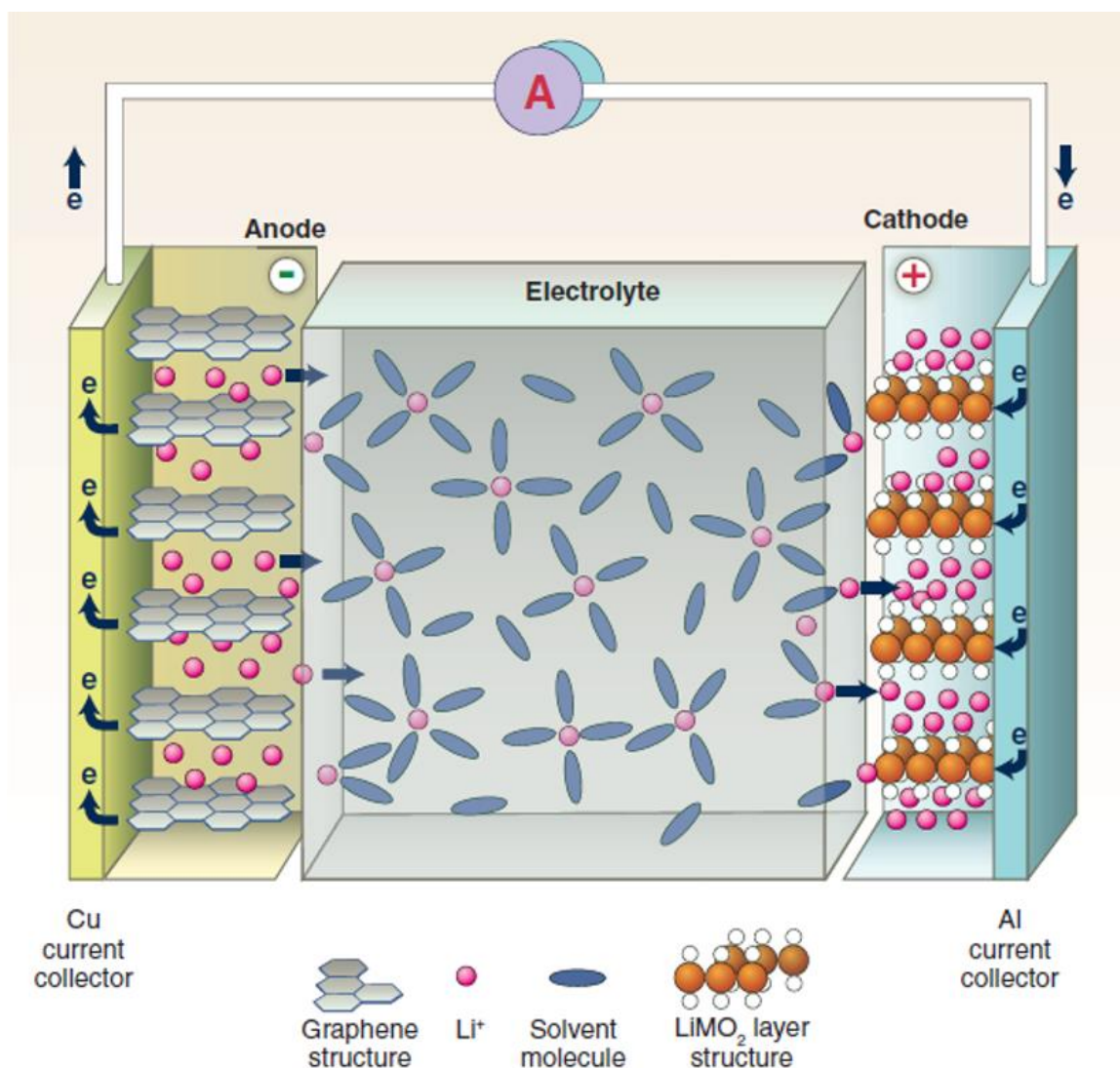


Figure 1.2. Lithium-Ion Battery Schematic. The Anode (Left) is Composed of a Copper Current Collector and Graphitic Carbon, Which Holds Lithium Ions. The Cathode (Right) Consists of an Aluminum Current Collector and a Lithium Metal Oxide Compound. The Lithium Ions are Transferred Between the Electrodes Via the Electrolyte That Utilizes an Organic Solvent to Shuttle the Ions.¹⁰

1.3 LIB Challenges

Presently, the lithium-ion battery is failing to satisfy the demands posed by current and developing technologies.⁸ In particular, its energy density, cost-effectiveness, and safety require improvement to match most energy storage needs.⁸ Currently, LIBs employ flammable organic solvents in their liquid electrolytes, which can catch fire during a battery malfunction. For example, there have been many accidents involving batteries within electric vehicles and cell phones which have ignited due to a short circuit.¹⁰ Not only do these safety issues pose a serious health risk to the consumer but they also significantly hurt company reputations. For example, Samsung lost \$10 billion to the exploding Galaxy Note 7.¹¹ Therefore, in order for the LIB to progress, its thermal stability must be drastically increased.

In addition to flammability, the carbonate solvents within liquid electrolytes prevent the use of lithium metal which has a theoretical capacity of $3840 \text{ mAh}\cdot\text{g}^{-1}$, ten times the theoretical capacity of graphite anodes.¹² The extreme reactivity of lithium metal with these solvents reduces capacity retention and increases safety risks.¹² Moreover, another downside of the liquid electrolyte is the requirement of the separator.⁴ Eliminating the need for the separator would reduce battery manufacturing cost and advance the manufacturing efficiency. Therefore, in order to propel the lithium-ion battery into the next generation, the liquid electrolyte needs to be replaced. An all-solid-state battery will not only dramatically improve the consumer electronics industry but it will also serve as a key development for all clean and sustainable energy technologies.

1.4 The Solid-State Battery

The achievement of an all-solid-state battery poses many challenges. One of the main struggles is the low ionic conductivity of solid-state electrolytes, which is several orders of magnitude below the ionic conductivity of an average liquid electrolyte. Most liquid electrolytes have an ionic conductivity of around $10^{-2} \text{ S}\cdot\text{cm}^{-1}$ at 25°C , while a solid-state electrolyte with $10^{-4} \text{ S}\cdot\text{cm}^{-1}$ ionic conductivity at room temperature is considered an achievement.^{13,14} This problem is further complicated by the need for sufficient mechanical strength ($\geq 30 \text{ MPa}$), which is required to prevent the formation of lithium dendrites.¹⁴ A proper balance of these two properties, as well as good thermal ($> 150^\circ\text{C}$) and electrochemical stability ($> 4 \text{ V vs. Li}^+/\text{Li}$), are the most sought features in solid-state electrolytes.¹⁴

There are several approaches taken in the development of SSEs, as shown in comparison in Table 1.1. However, most of them can be classified into the following two types: solid ceramic electrolytes (SCE) and solid polymer electrolytes (SPE).^{14,15} SCEs are inorganic and ceramic-based electrolytes that conduct ions through defects in their structure.^{14,15} As with most ceramics, they have excellent thermal stability, and they can attain high ionic conductivities.¹⁵ For example, the sulfur-based SCEs have been reported to exhibit an ionic conductivity of as high as $10^{-2} \text{ S}\cdot\text{cm}^{-1}$ at ambient temperature, which is comparable to liquid electrolytes.^{15,16} However, these electrolytes are unstable in contact with oxygen, requiring an argon atmosphere which poses significant difficulties in their synthesis and processing.¹⁷ Despite a lower ionic conductivity, oxide-based SCEs are a more popular approach since they do not require the use of the glovebox.^{14,15} But they

involve long calcination times at very high temperatures limiting their processability.¹⁷ In addition, SCEs are very brittle and suffer from high interfacial impedance with electrodes.^{17,19} Therefore, SCEs still require a lot of work before they can be used in batteries.

	SCE		SPE
	Oxide^{15,17}	Sulfide¹⁸	Polymer^{14,20}
Ionic Conductivity	Good, up to $10^{-4} \text{ S}\cdot\text{cm}^{-1}$	Excellent, up to $10^{-2} \text{ S}\cdot\text{cm}^{-1}$	Good, $10^{-6} \text{ S cm}^{-1}$ $10^{-3} \text{ S cm}^{-1}$ (Gel)
Thermal Stability	Excellent, > 500 °C	Good, > 300 °C	Poor, ~100 °C
Electrochemical stability	Good, >4V	Poor, <3V	Good, ~4V
Mechanical Strength	Hard and Brittle	Strong and ductile	Ductile but weak
Processability and Handling	High-temperature processing, easy to handle – air-stable	High-temperature processing, difficult to handle – control environment required	Low-temperature processing, easy to handle – air-stable

Table 1.1. Assessment of Different Solid Electrolyte Properties.

Solid polymer electrolyte (SPE) is another popular approach to achieve the solid-state battery. They consist of a polymer backbone and a lithium salt as an ion source, and they transfer lithium ions via polymer chain motion.^{14,20} Unlike the SCEs, they have great contact with electrodes, are easy to process, and are highly applicable and cost-effective.^{14,20} Despite their low conductivity, SPEs offer much potential due to their other benefits, and therefore many strategies have been developed in attempts to improve their conductivity. Since SPE ionic conduction stems from chain mobility, most strategies to improve this electrolyte concentrate on reducing the polymer's crystallinity.^{14,20} These strategies consist of designing polymer blends, adding plasticizers, and doping with fillers.^{14,20} Despite great efforts, the majority of the solid polymer electrolyte field is

standing on the ionic conductivity of $\sim 10^{-4} \text{ S}\cdot\text{cm}^{-1}$, which is two orders of magnitude below the liquid electrolyte.^{14,20} In order to achieve the liquid electrolyte level of ionic conductivity, another approach is needed. The more radical and less common approach involves the development of inorganic plastic crystal electrolytes (PCE).²¹⁻²³

1.5 Plastic Crystal Electrolytes

Plastic crystals are a class of materials that exhibit a phase that possesses rotational disorder while preserving long-range molecular order.^{21,24,25} This phase occurs in the transition between solid and liquid phases.²¹ In other words, the temperature threshold for orientational relaxation of these materials is lower than for their translational order relaxation. Unlike the glassy state, where both translational and rotational degrees of freedom are locked in place, the plastic crystal phase occurs when only translational degrees of freedom are reduced while the rotational degrees of freedom remain close to liquid level.^{21,26} In addition, the molecules in the plastic crystal lattice have weak mutual interactions which do not hinder molecular rotation.²⁵ The plastic crystal phase was first observed by Timmermans in the 1960s, who performed experiments on structurally simple compounds like cyclohexane which exhibits a plastic crystal phase between -87°C and 6°C where its globular structure rotates about an axis.²⁷⁻²⁹ However, plastic crystals have gained much popularity recently when it was found that this phase aids ion transfer.^{21,27}

Through current developments of various plastic crystal materials, two main groups can be established: molecular plastic crystals (cyclohexane, ethane, succinonitrile, etc.) and organic ionic plastic crystals (Li_2SO_4 , Na_3PO_4 , quaternary alkyl ammonium

systems, etc.).^{21,27} The former group is not intrinsically ionically conductive, while the latter exhibits intrinsic ionic conductivity.^{21,25,27} However, the ionic conductivity of both groups can be drastically enhanced by doping with ions.^{21,25,27} In both of these groups, the ion transfer mechanism is hypothesized to aid in three ways. 1) The reorientation of the molecules transfers ions through its rotator motion,^{21,27} 2) the reorientation creates defects in the lattice resulting in more free volume leaving more room for rotation and ion motion,²⁵ and 3) since the plastic crystalline phase nears translational degrees of freedom relaxation some molecules undergo translational motion across the lattice creating vacancies which ions can then fill.³⁰

Most popular organic ionic plastic crystals are salts composing of quaternary alkyl ammonium anion, pyrrolidinium cation, or imidazolium cation since these ionic moieties allow for the formation of the plastic crystalline phase.²⁷ Although they are intrinsically ionically conductive, they are commonly doped with ions to increase their conductivity further.²⁷ These plastic crystals can achieve high ionic conductivities of 10^{-3} S·cm⁻¹ at room temperature, have a wide electrochemical window of up to 6 V, and their thermal stabilities can reach 400 °C.^{31,32} However, its major disadvantage is its low mechanical stability at room temperature, which completely disintegrates with the addition of salt. Therefore, it cannot be used as a solid ion conductor on its own and needs a host matrix to achieve mechanical integrity.

The majority of recent research on ionically conductive molecular plastic crystals has been performed on succinonitrile (SN) doped with lithium salt.^{25,30,33} Succinonitrile consists of two nitrile groups freely rotating about the C-C bond.^{25,30,33} It has a body-

centered cubic (bcc) structure in its crystalline phase, and it exists in three isomeric confirmations: two *gauche* isomers, which are more abundant, and one *trans* isomer.³⁰ SN's nitrile groups are electronegative and possess a Gutmann donor number of 15, thereby attracting cations.³³ It experiences a plastic crystal phase between -35°C to 62°C; however, the addition of salt causes disorder in its lattice, which shifts this range to lower temperatures.³³ The magnitude of this shift is dependent upon the salt anion – larger anions cause more disorder, thereby increasing the shift. It can achieve ionic conductivities of as high as $10^{-3} \text{ S}\cdot\text{cm}^{-1}$ at room temperature, which is close to liquid electrolyte level, have a wide electrochemical voltage window of >5 V, especially useful for battery application, and is thermally stable with its boiling point being 267°C.³⁴ Other dinitriles, like malononitrile, glutaronitrile, and adiponitrile, also possess the plastic crystal phase, albeit at different temperature ranges.^{30,33-35} Glutaronitrile (GN) is a molecule of particular interest because it is very similar to succinonitrile in its composition and its properties; however, it has hardly been explored for the solid polymer electrolyte role.^{25,30} The main difference between GN and SN being an extra C-C bond that yields the GN molecule a larger size.^{25,30} GN has a plastic crystalline phase ranging from -60°C to -30°C, a wide electrochemical window of >6V, and a boiling point of 286°C.^{25,30} It also has a similar bcc crystal structure as succinonitrile.^{25,30} However, similar to organic ion plastic crystals, these plastic crystals also suffer from poor mechanical strength and require a host in order to be employed as a solid ion conductor.

1.6 Metal-Organic Frameworks

Metal-organic frameworks (MOFs) are crystalline structures consisting of metal ions bridged by organic ligands.^{39,40} They are a recently discovered class of coordination polymers and are known for their high surface area and tunability.^{39,40} The high surface area allows MOFs to have many reaction sites, which makes it an ideal candidate for catalysis, sensors, drug delivery vesicles, etc.³⁹ The tunability, which stems from a wide variety of metals and ligands that can be used to synthesize a metal-organic framework, permits MOFs to have optical and electrochemical properties to be perfectly tailored for each application.³⁹ These two aspects have opened a door of possibilities, and many never-before achieved technologies are now a reality. Therefore, there are many studies that analyze MOFs' nature; however, many more studies are needed in order for this material to achieve its full potential.

1.7 MOF Use in Lithium-Ion Batteries

Because of the aforementioned beneficial properties of organic metal frameworks, they are being considered for various roles within energy storage applications, with special focus paid to lithium-ion batteries.⁴⁰ Currently, MOFs are being examined for every major component of LIB: cathode, anode, and electrolyte.⁴⁰ For example, Hu *et al.* explore porous Co_3O_4 nanocages as a potential cathode material. The nanocages demonstrated a high and stable capacity of $1465 \text{ mAh}\cdot\text{g}^{-1}$ over 50 cycles at $300 \text{ mA}\cdot\text{g}^{-1}$, which was attributed to the small size, porous shell, and high surface area of the Co_3O_4 nanocages.⁴¹ Zhang *et al.* reported an anode material consisting of Fe_2O_3 microboxes with hierarchically structured shells, which showed a high specific capacity of $950 \text{ mAh}\cdot\text{g}^{-1}$ at

200 mA·g⁻¹, which was also credited to the porosity and high surface area of the microboxes.^{40,42}

MOFs are also showing promise in their use within electrolytes due to their low electrical conductivity, tunable polarity, and high porosity.⁴³ There are many ways that MOFs can be employed to elevate the downfalls of current electrolytes. For example, they can be used as hosts for liquid electrolyte solutions or ionic liquids. Long *et al.* first proposed the use of MOFs as a host for Li⁺ ions by absorbing a common electrolyte solution (1 M LiBF₄ in a 1:1 mixture of EC and DEC) within MOF-177. They were able to reach ionic conductivity values of 10⁻⁴ S·cm⁻¹ at 27 °C.^{44,45} However, the drying of the electrolyte solution within the MOFs presents an issue since the ion transport is mostly achieved by the solvent molecules within the electrolyte rather than by the MOF itself. Wang *et al.* impregnated metal-organic framework nanocrystals (Li-IL@MOF) with [EMIM_{0.8}Li_{0.2}][TFSI] ionic liquid, which achieved an ionic conductivity of 3.00 × 10⁻⁴ S·cm⁻¹ at ambient temperature in addition to stable LiFePO₄ half-cell performance for 100 cycles.⁴⁶ Furthermore, MOFs can also be used as a filler to reduce the crystallinity of SPEs. For example, Liu *et al.* utilized MOF-5 as a filler for a PEO/LiN(SO₂CF₃)₂ polymer electrolyte. This SPE reached an ionic conductivity of 3.16 × 10⁻⁵ S·cm⁻¹ at 25°C, which is ascribed to interactions among Lewis-acidic sites in MOF-5, N(SO₂CF₃)₂ and PEO chains, that not only inhibit the crystallization of PEO but also result in Li⁺ conducting paths on the surface of the filler.^{44,45}

Lastly, MOF itself can be used as a solid electrolyte.⁴⁷ One way to achieve this is with a lithium-based metal-organic framework (Li MOF), where excess lithium is

transferred through the defects in the MOF structure. However, research regarding Li MOFs as solid electrolytes is currently lacking. The majority of MOF/electrolyte studies are only focused on employing MOFs as a host of ionically conductive materials rather than utilizing MOFs as solid-state electrolytes. Therefore, in this study, we investigate the potential of Li MOF as a solid electrolyte. There are different types of Li MOFs already developed. Although many of them are designed for applications other than battery electrolytes, they are a good basis for this project because MOF structures can be tuned for lithium transport. For example, Zhao *et al.* reported a lithium cubane-based zeolitic framework possessing a multi-dimensional channel system intended for gas storage.⁴⁸ Banerjee *et al.* described the synthesis and structure of two Li MOFs: $\text{Li}_2(\text{C}_{14}\text{H}_8\text{O}_4)$ [$\text{Li}_2(4,40\text{-BPDC})$] and $\text{Li}_2(\text{C}_{14}\text{H}_8\text{O}_6\text{S})$ [$\text{Li}_2(4,40\text{-SDB})$].⁴⁹ Ogihara *et al.* studied electrical conductivity of lithiated 2,6-naphthalene dicarboxylate dilithium MOF designed for cathode material.⁵⁰ This paper is particularly interesting due to its use of lithiation. It demonstrates that Li MOF can be lithiated in order to provide excess lithium, which can travel through the structure. Overall, Li MOFs show potential for use as solid ionic conductors, and much research is needed to explore this possibility.

1.8 General Goal of Research

This dissertation work focused on investigating the potential of two novel paths of developing solid-state electrolytes using a novel system of plastic crystals (***Aim 1***) and a lithium-based metal-organic framework (Li-MOF) (***Aim 2***). In the utilization of plastic crystals, ***Aim 1*** studies the ion conduction mechanism of less-explored glutaronitrile (GN) plastic crystals in combination with polyacrylonitrile (PAN) as a polymer backbone

and lithium hexafluorophosphate (LiPF₆) as the lithium source. Additionally, the effect of plastic crystal has been studied with another lithium salt –lithium perchlorate (LiClO₃).

This aim tests the ion conduction mechanism of plastic crystal-based SPE that occurs through lattice defects created due to conformational transformations in glutaronitrile.

Unlike polyethylene oxide (PEO), polyacrylonitrile is not commonly used in SPEs due to its higher crystallinity; however, PEO was specifically chosen for this project due to its superb thermal stability (>300°C) and high electrochemical stability (>5 V).^{36,37} In addition, it possesses nitrile groups instead of the more electronegative oxygen groups, which would hijack the lithium ion from the less electronegative nitrile groups of glutaronitrile.³⁸ The lithium salt, LiPF₆, was also chosen because of the ease of its solubility and its lack of oxygen groups. Electrochemical, thermal, and mechanical characterizations were performed on the resulting electrolyte. The novelty of this study lies in the synthesis and characterization of the novel plastic crystal electrolyte in addition to the investigation of its ionic conduction mechanism.

Aim 2 explores the electrochemical properties of Li MOFs and their lithiated derivatives with a particular focus on their ionic and electrical conduction properties.

This aim tests the postulated hypothesis that MOFs can transfer Li⁺ ions through the carboxylic groups in their linkers while retaining their low electrical conductivity. A

novel lithium metal-organic framework consisting of lithium and biphenyl-4,4-dicarboxylic acid as a ligand is presented in this aim. In addition, a new, quick, environmentally friendly, and simple synthesis method is also proposed.

1.9 References

1. Rohde, R. A. & Muller, R. A. Air Pollution in China: Mapping of Concentrations and Sources. *PLoS One* **10**, e0135749 (2015).
2. Lutsey, N. *et al.* Power play: How governments are spurring the electric vehicle industry. (2018).
3. Randall, T. Here's How Electric Cars Will Cause the Next Oil Crisis.
4. Winter, M. & Brodd, R. J. What Are Batteries, Fuel Cells, and Supercapacitors? *Chem. Rev.* **104**, 4245–4270 (2004).
5. Megahed, S. & Scrosati, B. Lithium-ion rechargeable batteries. *J. Power Sources* **51**, 79–104 (1994).
6. Etacheri, V., Marom, R., Elazari, R., Salitra, G. & Aurbach, D. Challenges in the development of advanced Li-ion batteries: a review. *Energy Environ. Sci.* **4**, 3243 (2011).
7. Deng, D. Li-ion batteries: basics, progress, and challenges. *Energy Sci. Eng.* **3**, 385–418 (2015).
8. Scrosati, B., Hassoun, J. & Sun, Y.-K. Lithium-ion batteries. A look into the future. *Energy Environ. Sci.* **4**, 3287 (2011).
9. Dunn, B., Kamath, H. & Tarascon, J.-M. Electrical Energy Storage for the Grid: A Battery of Choices. *Science* (80). **334**, 928–935 (2011).
10. Görgülü, T., Torun, M. & Olgun, A. A cause of severe thigh injury: Battery explosion. *Ann. Med. Surg.* **5**, 49–51 (2016).
11. Mullen, J. & Thompson, M. Samsung takes \$10 billion hit to end Galaxy Note 7 fiasco. *CNNTech* (2016). Available at: <http://money.cnn.com/2016/10/11/technology/samsung-galaxy-note-7-what-next/index.html>. (Accessed: 26th June 2018)
12. Kozen, A. C. *et al.* Next-Generation Lithium Metal Anode Engineering via Atomic Layer Deposition. *ACS Nano* **9**, 5884–5892 (2015).

13. Kondo, K. *et al.* Conductivity and Solvation of Li⁺ Ions of LiPF₆ in Propylene Carbonate Solutions. doi:10.1021/jp000142f
14. Yue, L. *et al.* All solid-state polymer electrolytes for high-performance lithium ion batteries. *Energy Storage Mater.* **5**, 139–164 (2016).
15. Sun, C., Liu, J., Gong, Y., Wilkinson, D. P. & Zhang, J. Recent advances in all-solid-state rechargeable lithium batteries. *Nano Energy* **33**, 363–386 (2017).
16. Kato, Y. *et al.* High-power all-solid-state batteries using sulfide superionic conductors. *Nat. Energy* **1**, 16030 (2016).
17. Kerman, K., Luntz, A., Viswanathan, V., Chiang, Y.-M. & Chen, Z. Review—Practical Challenges Hindering the Development of Solid State Li Ion Batteries. *J. Electrochem. Soc.* **164**, A1731–A1744 (2017).
18. Tatsumisago, M., Nagao, M. & Hayashi, A. Recent development of sulfide solid electrolytes and interfacial modification for all-solid-state rechargeable lithium batteries. *J. Asian Ceram. Soc.* **1**, 17–25 (2013).
19. Tian, Y. *et al.* Compatibility issues between electrodes and electrolytes in solid-state batteries. *Energy Environ. Sci.* **10**, 1150–1166 (2017).
20. Ngai, K. S., Ramesh, S., Ramesh, K. & Juan, J. C. A review of polymer electrolytes: fundamental, approaches and applications. *Ionics (Kiel)*. **22**, 1259–1279 (2016).
21. Pringle, J. M.; Howlett, P. C.; Macfarlane, D. R.; Forsyth, M. Organic Ionic Plastic Crystals: Recent Advances. *J. Mater. Chem.* **2010**, 20, 2056–2062.
22. MacFarlane, R. D. and Forsyth, M. Plastic Crystal Electrolyte Materials: New Perspectives on Solid State Ionics. *Adv. Mater.* **2001**, 13
23. Hu, P. *et al.* Progress in nitrile-based polymer electrolytes for high performance lithium batteries. *J. Mater. Chem. A* **4**, 10070–10083 (2016).
24. Yvinec, M.; Pick, R. M. Orientational Disorder in Plastic Molecular Crystals I.-Group Theory and ODIC Description Orientational Disorder in Plastic Molecular Crystals I. 2014 Group Theory and ODIC Description. *J. Phys.* **1980**, 41 (9), 1045–1052.
25. Geirhos, K.; Lunkenheimer, P.; Michl, M.; Reuter, D.; Loidl, A. Conductivity Enhancement in Plastic-Crystalline Solid-State Electrolytes. *J. Chem. Phys.* **1** **2015**, 143 (081101).

26. Tyagi, M.; Murthy, S. S. N. Study of the Nature of Glass Transitions in the Plastic Crystalline Phases of Cyclo-Octanol, Cycloheptanol, Cyanoadamantane and Cis-1,2-Dimethylcyclohexane. *J. Chem. Phys.* **2001**, *114* (8), 3640–3652.
27. MacFarlane, R. D. and Forsyth, M. Plastic Crystal Electrolyte Materials: New Perspectives on Solid State Ionics. *Adv. Mater.* **2001**, *13*
28. Timmermans, J. Plastic Crystals: A Historical Review. *J. Phys. Chem. Solids* **1961**, *18* (1), 1–8.
29. Farman, H.; Coveney, F. M.; Dore, J. C. Structural Features of the Liquid/Plastic Crystal Phase Transition for Cyclohexane in Bulk and Confined Geometry. *Phys. B Condens. Matter* **1992**, *180–181*, 857–860
30. Zachariah, M.; Romanini, M.; Tripathi, P.; Barrio, M.; Tamarit, J. L.; Macovez, R. Self-Diffusion, Phase Behavior, and Li^+ Ion Conduction in Succinonitrile-Based Plastic Cocrystals. *J. Phys. Chem. C* **2015**, *119* (49), 27298–27306.
31. Jin, L.; Howlett, P. C.; Pringle, J. M.; Janikowski, J.; Armand, M.; MacFarlane, D. R.; Forsyth, M. An Organic Ionic Plastic Crystal Electrolyte for Rate Capability and Stability of Ambient Temperature Lithium Batteries. *Energy Environ. Sci.* **2014**, *7* (10), 3352–3361.
32. Villanueva, M.; Coronas, A.; García, J.; Salgado, J. Thermal Stability of Ionic Liquids for Their Application as New Absorbents. *Ind. Eng. Chem. Res.* **2013**, *52* (45), 15718–15727.
33. Alarco, P.-J.; Abu-Lebdeh, Y.; Abouimrane, A.; Armand, M. The Plastic-Crystalline Phase of Succinonitrile as a Universal Matrix for Solid-State Ionic Conductors. *Nat. Mater.* **2004**, *3* (7), 476–481.
34. Lv, P.; Li, Y.; Wu, Y.; Liu, G.; Liu, H.; Li, S.; Tang, C.; Mei, J.; Li, Y. Robust Succinonitrile-Based Gel Polymer Electrolyte for Lithium-Ion Batteries Withstanding Mechanical Folding and High Temperature. *ACS Appl. Mater. Interfaces* **2018**, *10* (30), 25384–25392.
35. Zhou, D.; He, Y.-B.; Liu, R.; Liu, M.; Du, H.; Li, B.; Cai, Q.; Yang, Q.-H.; Kang, F. In Situ Synthesis of a Hierarchical All-Solid-State Electrolyte Based on Nitrile Materials for High-Performance Lithium-Ion Batteries. *Adv. Energy Mater.* **2015**, *5* (15), 1500353.
36. Mindemark, J., Lacey, M. J., Bowden, T. & Brandell, D. Beyond PEO—Alternative host materials for Li^+ -conducting solid polymer electrolytes. *Prog. Polym. Sci.* **81**, 114–143 (2018).

37. Liang, Y. *et al.* Preparation and electrochemical characterization of ionic-conducting lithium lanthanum titanate oxide/polyacrylonitrile submicron composite fiber-based lithium-ion battery separators. *J. Power Sources* **196**, 436–441 (2011).
38. Sai, R. *et al.* Role of polar side chains in Li⁺ coordination and transport properties of polyoxetane-based polymer electrolytes. *Phys. Chem. Chem. Phys.* **19**, 5185–5194 (2017).
39. James, S. L. Metal-organic frameworks. *Chem. Soc. Rev.* **32**, 276 (2003).
40. Xu, G. *et al.* Exploring metal organic frameworks for energy storage in batteries and supercapacitors. *Mater. Today* **20**, 191–209 (2017).
41. Hu, L. *et al.* Fabrication Based on the Kirkendall Effect of Co₃O₄ Porous Nanocages with Extraordinarily High Capacity for Lithium Storage. *Chem. - A Eur. J.* **18**, 8971–8977 (2012).
42. Zhang, L., Wu, H. Bin, Madhavi, S., Hng, H. H. & Lou, X. W. Formation of Fe₂O₃ Microboxes with Hierarchical Shell Structures from Metal–Organic Frameworks and Their Lithium Storage Properties. *J. Am. Chem. Soc.* **134**, 17388–17391 (2012).
43. Zhao, R., Liang, Z., Zou, R. & Xu, Q. Metal-Organic Frameworks for Batteries. *Joule* **2**, 2235–2259 (2018).
44. Fu, X. *et al.* Inorganic and organic hybrid solid electrolytes for lithium-ion batteries. *CrystEngComm* **18**, 4236–4258 (2016).
45. Wiers, B. M., Foo, M.-L., Balsara, N. P. & Long, J. R. A Solid Lithium Electrolyte via Addition of Lithium Isopropoxide to a Metal–Organic Framework with Open Metal Sites. *J. Am. Chem. Soc.* **133**, 14522–14525 (2011).
46. Wang, Z. *et al.* A Metal-Organic-Framework-Based Electrolyte with Nanowetted Interfaces for High-Energy-Density Solid-State Lithium Battery. *Adv. Mater.* **30**, 1704436 (2018).
47. Yuan, C. *et al.* Enhanced electrochemical performance of poly(ethylene oxide) based composite polymer electrolyte by incorporation of nano-sized metal-organic framework. *J. Power Sources* **240**, 653–658 (2013).
48. Zhao, X. *et al.* A zeolitic porous lithium–organic framework constructed from cubane clusters. *Chem. Commun.* **47**, 5536 (2011).

49. Banerjee, D., Borkowski, L. A., Kim, S. J. & Parise, J. B. Synthesis and Structural Characterization of Lithium-Based Metal–Organic Frameworks. *Cryst. Growth Des.* **9**, 4922–4926 (2009).
50. Ogihara, N., Ohba, N. & Kishida, Y. On/off switchable electronic conduction in intercalated metal-organic frameworks. *Sci. Adv.* **3**, e1603103 (2017).

CHAPTER II

BACKGROUND

2.1 Ionic Conductivity Mechanism of SPES

The basic solid polymer electrolyte consists of a polymer host and an ion source, which is usually a salt.¹ Both play a role in ion transport, with the polymer host arguably having more of an influence on ion conduction.¹ Most polymers transfer ions by passing them via their functional groups from one chain to another, as shown in Figure 2.1 a).¹ The functional groups must be polar and have a sufficiently powerful electron donor in order to coordinate with lithium ions.² In addition, these groups must be highly mobile and have high bond rotation.^{2,3} Therefore, chain mobility is crucial to ionic conductivity.² Because of this, many techniques utilize polymers that are semi-crystalline or aim at reducing polymer crystallinity by combining it with another polymer or other additives.^{1,4} The salt properties and amount should also be optimized for the polymer host. The solubility of the salt, its ion size, and its thermal properties all affect SPE's ionic conductivity.³

There has been much research dedicated to deciphering the ion transport within polymers. This is a challenging topic because there are many material and external factors that influence ionic conductivity. Polymers are complicated materials because they exhibit complex phase diagrams, and their crystallinity varies with temperature.³ The majority of ion conduction occurs in the amorphous phase of the polymer.¹⁻⁵

Moreover, polymer's structure, molecular weight, and side groups also serve as key aspects in ion conduction. Additional complicating factors are the temperature-dependent ion pairing, as well as the degree of aggregation of ions which depend on both the polymer type and ion type.^{3,6} Since temperature has a profound influence on both the polymer and ions, it has a direct effect on ionic conductivity.

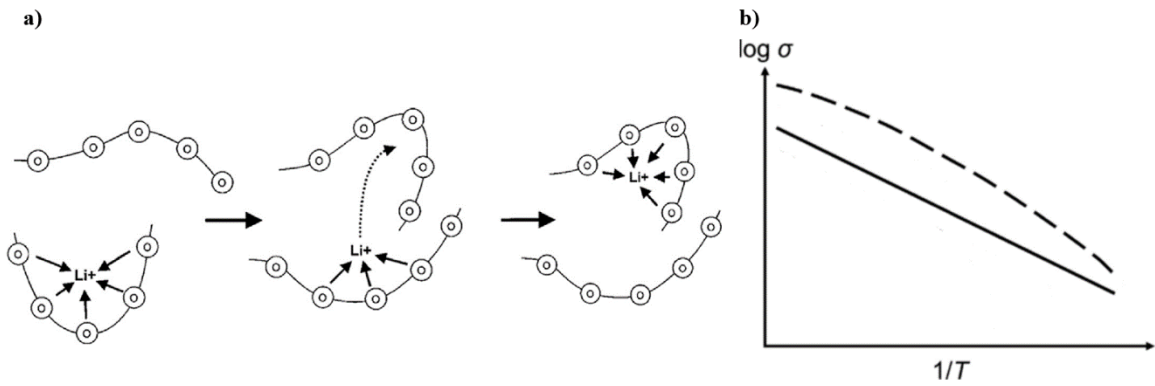


Figure 2.1 a) Li⁺ Transport Within a Polymer;¹ b) VFT (Dotted Line) and Arrhenius (Solid Line) Ion Conductivity Behavior.³

The most common model which describes SPE's relationship between temperature and ionic conductivity is the Vogel Fulcher Tamman (VFT) model, which is shown in Eq 2.1.^{3,6} A graph of this equation is shown in Figure 2.1 b).

$$\sigma = \sigma_0 \exp\left(\frac{-B}{T - T_0}\right), \quad \text{Eq. 2.1}$$

where σ is the ionic conductivity, σ_0 is a temperature-dependent pre-exponential factor ($\sigma_0 = AT^{-1/2}$), B is a factor associated with activation energy, and T_0 , also known as the 'Vogel temperature,' is a reference temperature related to the glass transition temperature (T_g).^{3,6} It refers to a temperature where the conductivity drops to zero.³ The VFT model

depicts the ionic conductivity in purely polymeric systems, and it correlates with the free volume theory, which describes polymeric motion in relation to the free space available. Most SPEs demonstrate a good fit to the VFT model, which means that the polymer is the dominant element of ion conduction.³ The VFT model shows that below T_g , the polymer has almost no conductivity and that increasing the amount of space within the polymer, e.g., using a plasticizer, can also increase ionic conduction.^{3,6}

Another common model used to describe the ionic conduction within SPEs is the Arrhenius equation shown in Eq. 2.2, where E_a is the activation energy and R is the gas constant.^{3,7} This model is used to describe ionic transport within liquid electrolytes. However, as SPE nears its glass transition temperature and the amount of the amorphous phase within the polymer increases, its ionic transport begins to resemble Arrhenius behavior, shown in Figure 2.1 b).^{3,8} Most SPEs exhibit both VFT and Arrhenius behavior at room temperature.^{3,8}

$$\sigma = \sigma_0 \exp \left(\frac{E_a}{RT} \right) \quad \text{Eq. 2.2}$$

2.2 Ionic Conductivity of MOFs

Coordination polymers (CPs) and metal-organic frameworks (MOFs) have also been considered for the role of ion conductors.⁹⁻¹⁵ Specifically, their ability to tune crystallinity, pore size, structure, and redox properties make MOFs attractive candidates for ion transport.^{9,10} Most common ion conductors researched are proton conductors, which are used in fuel cells and sensors, and lithium-ion conductors, which are crucial for energy storage.⁹⁻¹³ There are several approaches that can be taken to achieve ion

conductivity in MOFs. These approaches include: 1) encapsulating a solvent within the MOF structure to transport ions,⁹⁻¹¹ 2) employing defects in the MOF structure,^{9,12} 3) grafting of substituent groups onto the MOF channels to facilitate ion transport;^{9,13} and 4) synthesizing novel MOF systems which contain the ion within its structure.^{14,15}

The use of an ionically conductive solvent to transport ions within MOFs is the most popular method to enhance their ionic conductivity.⁹⁻¹¹ For example, Meng *et al.* synthesized a novel MOF structure with high proton conductivity of up to $0.95 \times 10^{-2} \text{ S}\cdot\text{cm}^{-1}$ at 60°C and 97% relative humidity.¹¹ The high relative humidity allows for water molecules to be captured by the MOF, which transfers ions via the Grotthuss and Vehicular processes.¹¹ The Grotthuss mechanism, shown in Figure 2.2, involves proton hopping between water molecules, which induces molecular rotation.¹⁶ Subsequently, this molecular rotation allows for the next jump.^{16,17} The Vehicular mechanism involves an excess proton traveling to the top of the host molecule through the solvent.^{16,17} These two mechanisms are the most common transfer method of protons within water.

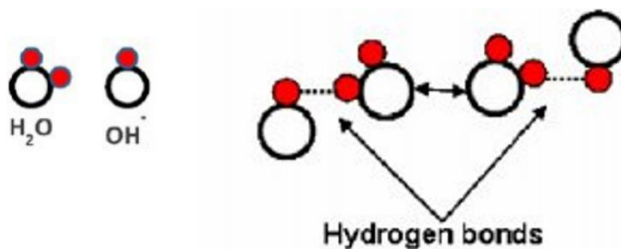


Figure 2.2. A Schematic of the Grotthuss Mechanism.¹⁷

Lithium ion conductivity of numerous MOFs has also been assessed using various solvents. For instance, Fujie *et al.* investigated lithium-ion transport in a system

constituting of an ionic liquid (mixture of EMI-TFSA (1-ethyl-3-methylimidazolium bis(trifluoromethylsulfonyl)-amide) with LiTFSA (lithium bis(trifluoromethylsulfonyl)amide)) incorporated into ZIF-8.¹⁰ They found that by reducing the size of MOF micropores, they were able to lower the freezing point of the ionic liquid, thereby increasing ionic conductivity.¹⁰ This occurred because the micropores were too small for the large ionic liquid molecules to aggregate.¹⁰ Fujie *et al.* draw an important conclusion that the pore size and structure of the MOF plays a crucial role in ionic conduction.^{9,10}

The utilization of defects within MOFs for ionic transport has also been investigated as a means to improve ionic conductivity.^{9,12} Taylor *et al.* demonstrate that by controlling the defect composition in UiO-66 through the addition of long-chain fatty acids to the synthesis, the proton conductivity can be increased by nearly three orders of magnitude to reach $6.79 \times 10^{-3} \text{ S}\cdot\text{cm}^{-1}$ at high humidity.¹² This occurred due to increases in both charge carrier concentration and mobility.¹² However, similar to the Meng *et al.* study, the Grotthuss and Vehicular mechanism remained the major means of ion transport in this system.¹²

Grafting substituent groups within the MOF channels have also been examined for ion transport.^{9,13} Ameloot *et al.* describe a novel two-step procedure involving dehydration of inorganic clusters of UiO-66, followed by lithium alkoxide grafting onto the framework, which leads to an ionic conductivity of $1.8 \times 10^{-5} \text{ S}\cdot\text{cm}^{-1}$, which is four times higher than the un-grafted sample.¹³ The insertion of the tBuO^{-1} anion into MOF allowed for increased lithium ion hopping within the framework.¹³ This study reveals the

potential of how the addition of various functionalities onto MOFs can yield novel ion conductors.

Lastly, another method to induce ionic transport within MOFs utilizes the metals which are already in the structure, one of the most common examples being lithium MOFs (Li MOFs).^{9,14,15} For example, Banerjee *et al.* synthesized and investigated the structure of two Li MOFs: $\text{Li}_2(\text{C}_{14}\text{H}_8\text{O}_4)$ [$\text{Li}_2(4,40\text{-BPDC})$] and $\text{Li}_2(\text{C}_{14}\text{H}_8\text{O}_6\text{S})$ [$\text{Li}_2(4,40\text{-SDB})$].¹⁴ The presence of lithium and carboxylic groups within the structure provide a potential pathway for lithium ions to travel through the framework. However, in this particular study, the Li MOF structure is very stable and therefore does not allow for the lithium ions to leave their sites. In fact, the stability of most Li MOF systems is an issue for ion conductivity since lithium ions are strongly bonded to their ligands and thereby cannot travel freely within the framework. One of the ways to introduce free lithium ions into the MOF is through lithiation, as shown in the Ogihara *et al.* study.¹⁵ They utilize a layered structure of 2,6-naphthalene dicarboxylate dilithium, which they lithiate using a tert-Butyllithium reflux reaction.¹⁵ As a result, they were able to achieve ionic conductivities of $10^{-5} \text{ S}\cdot\text{cm}^{-1}$ at room temperature.¹⁵ The lithium ion, added through lithiation, was able to travel via carboxylic groups within the structure.¹⁵

2.3 Ionic Conductivity Measurements

Electrochemical impedance spectroscopy (EIS) is the standard method for ionic conductivity measurement.^{1,2} It is a multifaceted technique that uses an AC signal at varying frequencies to monitor the impedance response of the system.¹⁸⁻²⁰ The oscillating electric field from the AC signal allows for charge transfer within the sample material,

while the number of charges transferred depends on the signal's frequency.¹⁹ The most common plot resulting from this measurement is referred to as the Nyquist plot, shown in Figure 2.3 a).^{18,19}

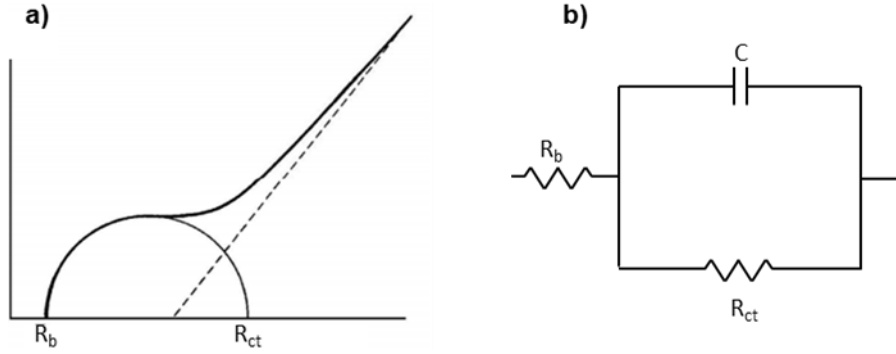


Figure 2.3. a) Typical Shape of a Nyquist Plot; b) Model Circuit Used to Fit the Nyquist Plot Shown in a).

The point where the semicircle intersects with the real axis of impedance is the bulk resistance of the system, R_b .^{18,19} The second point where the semicircle intersects the real axis is the charge transfer resistance, R_{ct} .^{18,19} In our case, R_{ct} represents the resistance within the sample and electrode interface. Lastly, the angle of the line corresponds to charge diffusion between the sample and electrode.^{18,19} In order to extrude these values from a typical Nyquist plot, the data needs to be fitted onto a model circuit, Figure 2.3 b).^{18,20} The bulk resistance value can then be used to calculate the ionic conductivity of the sample, σ , as shown in Eq. 2.3.^{1,2,18-20}

$$\sigma = \frac{L}{R_{BS}}, \quad \text{Eq. 2.3}$$

where L is the thickness of the sample, S is its area, and R_b is its bulk resistance. Standard parameters of this experiment involve a voltage amplitude of 10 mV and a frequency range of 10 Hz to 1 MHz.^{1,2}

2.4 References

1. Yue, L. *et al.* All solid-state polymer electrolytes for high-performance lithium ion batteries. *Energy Storage Mater.* **5**, 139–164 (2016).
2. Aziz, S. B., Woo, T. J., Kadir, M. F. Z. & Ahmed, H. M. A conceptual review on polymer electrolytes and ion transport models. *J. Sci. Adv. Mater. Devices* **3**, 1–17 (2018).
3. Mindemark, J., Lacey, M. J., Bowden, T. & Brandell, D. Beyond PEO—Alternative host materials for Li⁺-conducting solid polymer electrolytes. *Prog. Polym. Sci.* **81**, 114–143 (2018).
4. Sun, C., Liu, J., Gong, Y., Wilkinson, D. P. & Zhang, J. Recent advances in all-solid-state rechargeable lithium batteries. *Nano Energy* **33**, 363–386 (2017).
5. MacGlashan, G. S., Andreev, Y. G. & Bruce, P. G. Structure of the polymer electrolyte poly(ethylene oxide)₆:LiAsF₆. *Nature* **398**, 792–794 (1999).
6. Hallinan, D. T. & Balsara, N. P. Polymer Electrolytes. *Annu. Rev. Mater. Res.* **43**, 503–525 (2013).
7. Shangguan, Y. *et al.* New Insight into Time-Temperature Correlation for Polymer Relaxations Ranging from Secondary Relaxation to Terminal Flow: Application of a Universal and Developed WLF Equation. *Polymers (Basel)*. **9**, 567 (2017).
8. Petrowsky, M. & Frech, R. Temperature Dependence of Ion Transport: The Compensated Arrhenius Equation. *J. Phys. Chem. B* **113**, 5996–6000 (2009).
9. Horike, S., Umeyama, D. & Kitagawa, S. Ion Conductivity and Transport by Porous Coordination Polymers and Metal–Organic Frameworks. *Acc. Chem. Res.* **46**, 2376–2384 (2013).
10. Fujie, K., Ikeda, R., Otsubo, K., Yamada, T. & Kitagawa, H. Lithium Ion Diffusion in a Metal–Organic Framework Mediated by an Ionic Liquid. *Chem. Mater.* **27**, 7355–7361 (2015).
11. Meng, X., Wei, M.-J., Wang, H.-N., Zang, H.-Y. & Zhou, Z.-Y. Multifunctional luminescent Zn (ii)-based metal–organic framework for high proton-conductivity and detection of Cr³⁺ ions in the presence of mixed metal ions. *Dalt. Trans.* **47**, 1383–1387 (2018).

12. Taylor, J. M., Dekura, S., Ikeda, R. & Kitagawa, H. Defect Control to Enhance Proton Conductivity in a Metal–Organic Framework. *Chem. Mater.* **27**, 2286–2289 (2015).
13. Ameloot, R. *et al.* Ionic Conductivity in the Metal-Organic Framework UiO-66 by Dehydration and Insertion of Lithium *tert* -Butoxide. *Chem. - A Eur. J.* **19**, 5533–5536 (2013).
14. Banerjee, D., Borkowski, L. A., Kim, S. J. & Parise, J. B. Synthesis and Structural Characterization of Lithium-Based Metal–Organic Frameworks. *Cryst. Growth Des.* **9**, 4922–4926 (2009).
15. Ogihara, N., Ohba, N. & Kishida, Y. On/off switchable electronic conduction in intercalated metal-organic frameworks. *Sci. Adv.* **3**, e1603103 (2017).
16. Ludueña, G. A., Kühne, T. D. & Sebastiani, D. Mixed Grotthuss and Vehicle Transport Mechanism in Proton Conducting Polymers from Ab initio Molecular Dynamics Simulations. *Chem. Mater.* **23**, 1424–1429 (2011).
17. Merle, G., Wessling, M. & Nijmeijer, K. Anion exchange membranes for alkaline fuel cells: A review. *J. Memb. Sci.* **377**, 1–35 (2011).
18. Reece, C. *An Introduction to Electrochemical Impedance Spectroscopy*, (Jefferson Labs, 2010).
19. Barsoukov, E. and Macdonald, J. R. (James R. *Impedance spectroscopy : theory, experiment, and applications*. (Wiley-Interscience, 2005).
20. Lasia, A. in *Modern Aspects of Electrochemistry* (ed. Conway, B. E.) 143–248 (Kluwer Academic Publishers, 1999). doi:10.1007/0-306-46916-2_2

CHAPTER III

EXPERIMENTAL

3.1 Materials

The following section provides a description of all materials used in this work. Unless otherwise stated, all materials are used without any alterations.

Polyacrylonitrile (PAN, MW 150,000) was purchased from Sigma Aldrich. Ethylene carbonate (EC, 99% purity) was purchased from Sigma-Aldrich. Lithium hexafluorophosphate (LiPF_6 , 99% purity) was purchased from Sigma-Aldrich. Glutaronitrile (GN, 99% purity) was purchased from Alfa Aesar. Alumina nanopowder, 13 nm primary particle size (TEM), 99.8% trace metals basis (Al_2O_3 , 99.8% purity), was purchased from Sigma Aldrich. Lithium perchlorate (LiClO_4 , 96% purity) was acquired from Acros Organics. Lithium hexafluorophosphate solution in ethylene carbonate and diethyl carbonate, 1 M LiPF_6 -EC-DEC (1:1 vol%), battery grade, was purchased from Sigma Aldrich. $\text{LiNi}_{0.6}\text{Mn}_{0.2}\text{Co}_{0.2}\text{O}_2$ (NMC622), battery grade, active material was purchased from Umicore/Palm Commodities International. Lithium titanate $\text{Li}_4\text{Ti}_5\text{O}_{12}$ (LTO), battery grade, was acquired from MTI Corporation. Carbon black filler (Super C65), battery grade, acquired from Timcal Imerys. Polyvinylidene fluoride (PVDF, 99.8% purity), purchased from Solvay. 1-methyl-2-pyrrolidinone, anhydrous, (NMP, $\geq 99.5\%$ purity) acquired from Sigma Aldrich. Artificial graphite, 19.0 - 23.0 μm particle distribution, battery grade, purchased from Sigma Aldrich. A C480 separator was

purchased from Celguard. Stainless steel 2032 coin cell parts purchased from Linyi Gelon. Carboxymethyl cellulose (CMC) binder, battery grade, acquired from MTI Corporation. Styrene-Butadiene Rubber (SBR) binder purchased from MTI Corporation. Aluminum (Al) foil, 7 μm thick, battery grade, was purchased from MTI Corporation. 14 μm thick battery-grade copper (Cu) foil was also purchased from the MTI Corporation. 4 mm aluminum tabs and 4 mm nickel tabs were acquired from the MTI Corporation. The laminated aluminum pouch cell casing material was purchased from the MTI Corporation. Lithium perchlorate (LiClO_4 , 96% purity) was purchased from Acros Organics. Tetrahydrofuran, anhydrous (THF) was purchased from Sigma Aldrich. Polyvinylpyrrolidone (PVP, 40,000 MW) was purchased from Sigma Aldrich. N,N-dimethylformamide, anhydrous (99.8% purity) was purchased from Sigma Aldrich. Zinc acetate dihydrate and 2,6-naphthalenedicarboxylic acid (NDCA, 95% purity) were purchased from Sigma Aldrich. Biphenyl-4,4'-dicarboxylic acid (BDCA, 97% purity) was acquired from Sigma Aldrich. Lithium hydroxide monohydrate ($\text{LiOH}\cdot\text{H}_2\text{O}$, 56.5% min) was purchased from Alfa Aesar.

3.2 Characterization

The following section lists the characterizations used in this study.

Ionic conductivity data were collected with VMP3 Bio-Logic multichannel potentiostat. The ionic conductivity measurements were performed using electrochemical impedance spectroscopy (EIS). First, the surface area of the sample was measured with calipers. Next, its thickness was measured with a micrometer. Lastly, the sample was sandwiched between two gold-coated 25 mm diameter copper disks, which were

connected to an alternating current with a 10 mV amplitude and a varying frequency range of 10 Hz to 1 MHz. ZView software was used to fit EIS data and determine the bulk resistance, R_b , of the sample. The ionic conductivity and activation energy values were calculated using equations described in Chapter 2. Electrochemical stability data was collected with VMP3 Bio-Logic multichannel potentiostat. The sample was sandwiched between two gold-coated 25 mm diameter copper disks, which were connected to a potentiostat. Linear sweep voltammetry (LSV) was then performed using a scanning rate of 10 mV/s and lithium metal as the counter, reference, and working electrodes. In addition, cyclic voltammetry (CV) was conducted for 5 cycles using the same conditions as LSV. A 0 to 5 V range, with respect to open-circuit voltage, was used. Thermal stability was investigated by measuring a 10 mg of sample and placing it into the TA Instruments TGA Q500 thermogravimetric analyzer. A scanning rate of 10°C/min, a temperature range of 15°C to 350°C, and a nitrogen atmosphere were employed in this procedure. For a control sample, a liquid electrolyte, 1 M LiPF₆-EC-DEC (1:1 vol%), and a saturated separator were used. Compositional analysis was conducted using Varian 670 Fourier Transform Infrared (FTIR). A resolution of 8 cm⁻¹ at a sensitivity of 1.5 and a range of 400 to 4000 cm⁻¹ were used in this experiment. Additionally, compositional data were also collected using energy dispersive x-ray spectroscopy (EDX) with a 12 keV accelerating voltage and an 8.5 mm working distance. The morphological properties of the SPE were assessed via a Zeiss Auriga field emission scanning electron microscope (SEM) using a working distance of 5 mm and an accelerating voltage of 5 kV. Leica ACE200 Sample Coater was used to coat SEM

samples with gold palladium. Rigaku (Oxford) Gemini X-Ray Diffractometer with Mo and Cu sources was used for XRD data collection. An exposure time of 60 s was used with a working distance of 55 mm for all samples. A Toyo TOSCAT-3200 hundred channel battery cycler was used in combination with the Tenney environmental chamber for battery cycling. The formation cycle involved a current rate of 0.01C charge and discharges for both coin and pouch cell batteries. Cycling current rates ranged from 0.3 to 2C. The mechanical integrity of the SPE membrane was determined through tensile testing with Instron Material Test Frame 5900R. A gauge length of 2 cm and a rate of 6 mm/min were used on a 4 cm × 1 cm piece of polymer electrolyte.

3.3 Experimental Procedures

The following section describes the experimental procedures used in this study.

Experiment 3.1.1: Bare and Alumina-SPE synthesis

There are two types of membranes synthesized in this work: bare-SPE (LiPF₆/PAN/GN) and Alumina-SPE (LiPF₆/PAN/GN/Al₂O₃). The bare membrane does not contain any fillers, while the latter employs alumina nanoparticles to improve thermal and mechanical stability.

Bare-SPE was synthesized by adding polyacrylonitrile to melted ethylene carbonate to form a 12% solution. The mixture was stirred using a magnetic stirrer at 80°C for 3 hours. Next, 5.6wt% of Lithium hexafluorophosphate was mixed with melted EC to form a 24% solution, and once the salt had been dissolved, the solution was added into the 12% PAN/EC mixture and stirred at 80°C for 1 hour. Next, 18.4wt% of glutaronitrile was added, and the solution was stirred at the same conditions for an

additional hour. The mixture was then cast onto aluminum foil using a doctor blade.

Lastly, the cast electrolyte was dried for 12 hours at ambient temperature. To improve the properties of the SPE, 3wt% of Al_2O_3 was mixed with the solution prior to casting via ball milling to form an Alumina-SPE. Zirconia balls 5 mm in diameter were used at 3/1 solution per ball mass ratio. The solution was ball milled for 30 minutes at 800 rpm. After ball milling, it was cast onto aluminum foil using a doctor blade and was dried for 12 hours at ambient temperature, similarly to the bare-SPE.

Experiment 3.1.2: Electrode preparation

The coin cells 2032 with $\text{LiNi}_{0.6}\text{Mn}_{0.2}\text{Co}_{0.2}\text{O}_2$ (NMC622) as the cathode and artificial graphite as an anode were assembled. The full cell was tested in both coin cell and pouch cell configurations at 0.1 C formation and 0.3C cycling. All testing has been conducted at room temperature.

The ingredients for the cathode material slurry comprise 94wt% of NMC622, 3wt% C-65 as conductive carbon, and 3wt% binder. The binder was synthesized using polyvinylidene fluoride that was dissolved in 1-methyl-2-pyrrolidinone solvent. The slurry was cast on 7 μm thick battery-grade Al foil using a doctor blade and vacuum drawdown coater to result in roughly the same loading per unit area of active material. Initially, the laminates were dried slowly in air and at room temperature. As the final step, they were dried at 110°C under vacuum for 10 hrs.

The anode material slurry for the negative electrode was prepared with 94wt% of artificial graphite, 2wt% conductive carbon, 2wt% carboxymethyl cellulose (CMC) binder, and 2wt% Styrene-Butadiene Rubber (SBR) binder. All electrode laminates were

cast on 14 μm thick battery-grade Cu foil using a doctor blade and a vacuum drawdown coater such that the loading per unit area of active material is uniform. The laminates were first dried slowly at atmospheric pressure and room temperature; then, they were dried further at 110°C under vacuum for 10 hrs.

Experiment 3.1.3: Coin and pouch cell assembly

Coin cells 2032 were assembled using the LTO electrode prepared above as the cathode, lithium metal (0.25 mm thickness) as the anode, a C480 separator, and the solid electrolyte membrane. A control cell was prepared as described above, substituting SPE membrane with a liquid electrolyte, 1 M $\text{LiPF}_6/\text{EC}/\text{DEC}$, where EC:DEC was used at a 1:1 volume ratio. After preparation, the coin cells were left to sit in a cycler at room temperature for 10 hours.

The electrodes were then cut into rectangular pieces: the cathode cut 26 x 38 mm and the anode cut 28 x 40 mm. A 4 mm aluminum tab was ultrasonically welded onto the cathode piece, and a 4 mm nickel tab was ultrasonically welded onto the anode piece. The electrodes were then moved into the argon glovebox for pouch cell assembly. Inside an argon glove box, a 32 x 44 mm piece of the solid electrolyte membrane was placed atop the anode and the cathode placed atop the membrane. The assembly was then sandwiched between four ethyl vinyl acetate layers (30 x 42 x 1 mm). The whole complex was wrapped with a 40 x 100 mm C480 separator. The ends of the assembled cell were taped with Kapton tape, and it was placed in an aluminum laminated pouch cell case (110 mm x 110 mm). Each side of the pouch cell was sealed using an 8 inch Manual Hand Sealer. The pouch was then transferred out of the glovebox and vacuum-sealed

using a VacMaster VP210 (VacMaster). The pouch cells were left to sit in the cycler at ambient conditions (room temperature) for 10 hrs.

Experiment 3.2.1: LiClO₄/Glutaronitrile solution synthesis

The relationship between lithium ions and glutaronitrile was first investigated within solutions of varying LiClO₄ concentration – 2mol% (0.023 mg), 3mol% (0.035 mg), 4mol% (0.047 mg), 5mol% (0.059 mg) and 6mol% (0.072 mg) for 1 mL of GN. The solutions were synthesized by combining lithium perchlorate with glutaronitrile and magnetically stirring for 12 hours at 80°C.

Experiment 3.2.2: LiClO₄/PAN/GN synthesis

The solid polymer electrolyte (SPE) was synthesized by adding 0.282 g of polyacrylonitrile (PAN, MW 150,000. Sigma Aldrich) to 1.098 g of melted ethylene carbonate (EC, 99% Sigma-Aldrich) to form a 26% solution. The mixture was stirred using a magnetic stirrer at 80°C for 3 hours. Next, the 500 µL of each of the LiClO₄/GN solutions described above were added to 1.38 g of PAN/EC mixture and stirred at 80°C for 1 hour. A LiClO₄-free control sample was synthesized by mixing 500 µL of GN with 1.38 g of PAN/EC. Additionally, GN-free control samples were also synthesized by mixing the following amount of LiClO₄ with 1.38 g of PAN/EC: 2mol% (0.012 mg), 3mol% (0.018 mg), 4mol% (0.024 mg), 5mol% (0.030 mg) and 6mol% (0.036 mg). The mixtures were then cast either onto aluminum foil or onto an ITO substrate. Lastly, the cast electrolyte was dried in the nitrogen glove box for 12 hours at 100°C temperature.

Experiment 3.2.3: IV plot measurement of LiClO₄/PAN/GN

To examine the IV plot characteristic of SPE membranes, devices consisting of an ITO substrate, a 1 mm layer of SPE membrane, and 100 nm copper electrodes were synthesized. The ITO substrates were cleaned via 15 min sonication in IPA and water, respectively. The substrates were then dried with nitrogen and subjected to UV cleaning for 30 min. The polymer solution was then spin-coated onto the pristine substrates within a nitrogen atmosphere using a duration of 1 min at 3000 rpm with a 500 rpm acceleration and deceleration. The substrates were heated at 100°C for 12 hours to evaporate the solvent. The 100 nm copper electrodes were deposited onto the substrate using physical vapor deposition (Kurt Lesker PVD-75). The final device had an active area of 4.75 cm² and a 2.5 cm² channel length. The conductivity was obtained from Eq. 3.1.

$$\rho = \frac{Gl}{A}, \quad \text{Eq. 3.1}$$

where ρ is conductivity, G is conductance obtained from the slope of the ohmic region, and l and A are channel length and area, respectively.

Experiment 3.3.1: Zn MOF Synthesis

Zinc metal organic frameworks (Zn MOFs) were synthesized using the solvothermal process described below. A precursor mixture of zinc acetate (0.400 mmol) and 2,6-Naphthalenedicarboxylic acid (0.800 mmol) was combined with 1 mL of anhydrous N,N-Dimethylformamide in a small porcelain crucible. The mixture was stirred, covered with aluminum foil, and heated at 260°C for 7 minutes. The product was collected from the aluminum foil and centrifuged with acetone to remove the residual

solvent. The product was dried at room temperature resulting in a crystalline powder (33% w/w% yield). The FTIR spectra of the Zn MOFs demonstrated the following peaks: 3158 cm^{-1} (OH), 1695 cm^{-1} (carboxylate carbonyl), 1540 to 1600 cm^{-1} (aromatic C=C bonds), and 1400 – 1355 (C-O-Zn).

Experiment 3.3.2: Pellet pressing

In order to perform ionic conductivity measurements, as described in the characterization section of this chapter, a Zn MOF pellet was made by placing ~0.5 g of dry Zn MOF powder into a stainless-steel mold and pressing it at 5 tons for 1 minute. The pellet had a diameter of 19 mm and a thickness ranging from 0.8 to 0.5 mm.

Experiment 3.3.3: Addition of electrolytic solutions to Zn MOF pellet

In order to improve the ionic conductivity of the Zn MOF, various electrolytic solutions were drop-cast onto the Zn MOF pellet. The solutions used are as follows: 10wt% $\text{LiClO}_4/\text{DMF}$, 10wt% $\text{LiClO}_4/\text{THF}$, and ~6wt% LiClO_4/GN . The DMF and THF solutions were synthesized by combining lithium perchlorate with the respective solvent and magnetically stirring for 1 hour at room temperature. Due to the lower solubility of LiClO_4 in GN, this solution had to be synthesized by combining LiClO_4 with GN and magnetically stirring for 12 hours at 80°C. The solutions were utilized directly after their synthesis to reduce lithium's exposure to moisture. The solutions were drop-cast onto the pellet in 10 μL increments, with 50 μL being the highest amount, and ionic conductivity was measured after each increment.

Experiment 3.3.4: Li MOF_NDCA synthesis

The Li MOF_NDCA were synthesized using a solvothermal method. Lithium hydroxide hydrate (0.477 mmol) was combined with 2,6-Naphthalenedicarboxylic acid (0.477 mmol) and 1 mL of anhydrous N,N-Dimethylformamide in a small porcelain crucible. The mixture was stirred, covered with aluminum foil, and heated at 260°C for 7 minutes. The product was collected from the aluminum foil and dried under a vacuum at room temperature to protect the powder from moisture. The FTIR spectra of the Li MOF_NDCA demonstrated the following peaks: 3300 – 2500 cm^{-1} (OH), 1673 cm^{-1} (carboxylate carbonyl), and 1596 cm^{-1} (aromatic C=C bonds), and 1296 cm^{-1} (C-O).

Experiment 3.3.5: Li MOF_BDCA synthesis

The Li MOF_BDCA were synthesized using a solvothermal method. Lithium hydroxide hydrate (0.357 mmol) was combined with Biphenyl-4,4'-dicarboxylic acid (0.477 mmol) and 1 mL of anhydrous N,N-Dimethylformamide in a small porcelain crucible. The mixture was stirred, covered with aluminum foil, and heated at 250°C for 7 minutes. The product was collected from the aluminum foil and dried under a vacuum at room temperature to protect the powder from moisture. The FTIR spectra of the Li MOF_BDCA demonstrated the following peaks: 3300 – 2500 cm^{-1} (OH), 1666 cm^{-1} (carboxylate carbonyl), and 1596 cm^{-1} (aromatic C=C bonds), and 1280 cm^{-1} (C-O).

CHAPTER IV

RESULTS AND DISCUSSION

This chapter discusses the results achieved in this study.

4.1 LiPF₆/GN/PAN/EC Electrolyte System

This section addresses *Aim 1* of the study, and it discusses glutaronitrile's (GN) role in ion conduction within the first SPE system comprising of lithium hexafluorophosphate (LiPF₆) as the lithium salt and polyacrylonitrile (PAN) as the mechanical backbone. Experimental procedures pertaining to this section are described in 3.1.1–3.1.3.

4.1.1 Lithium Ion Conduction Mechanism Within LiPF₆/GN/PAN/EC System

Figure 4.1 a) and b) show the photos of the Alumina-SPE membrane. Upon doctor blade casting and drying, the membrane results in a transparent, thin (~50 - 40 μm) and flexible film shown in Fig. 4.1 a) and b). Figure 4.1 c) – f) demonstrate the SEM images of the bare and Alumina-SPE. The bare membrane displays dense and rough surface morphology with no pinholes. The Alumina-SPE also does not contain any pinholes; however, it possesses a visibly smoother surface. This coincides with prior research, which shows that the addition of a filler to a polymer electrolyte results in a more even topology.^{1,2} This trend is indicative of a reduction in crystallinity which occurs due to Alumina nanoparticles inhibiting polymer chain nucleation.^{1,2} This is a well-researched phenomenon and is commonly utilized to increase the amorphousness of the

polymer, which in turn improves its ionic conductivity.¹⁻³ The roughness of the membrane surface indicates that the electrolyte is most likely amorphous, despite PAN being known as a semi-crystalline polymer.²⁻⁴

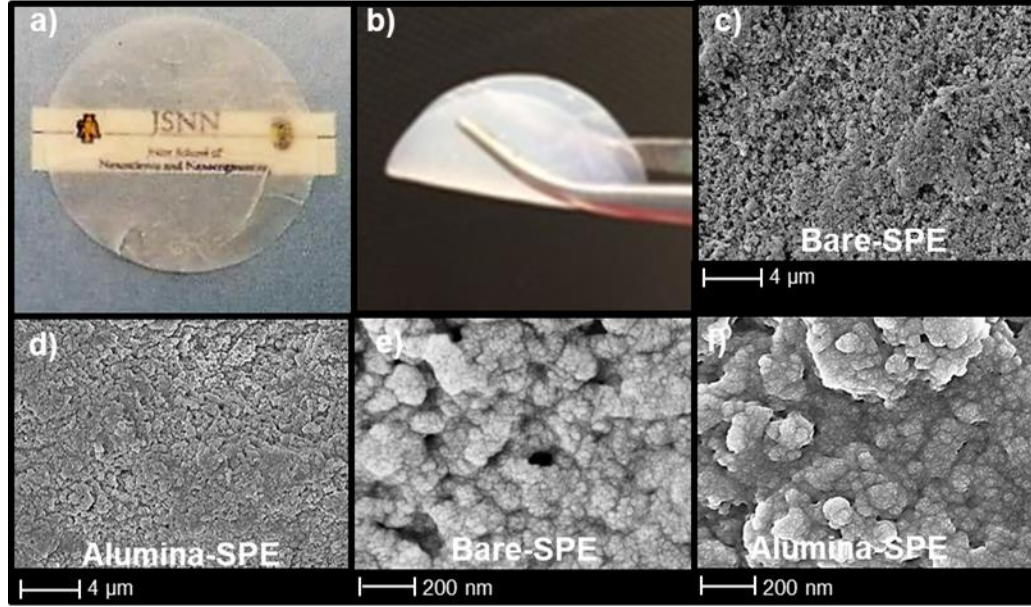


Figure 4.1 a) Photograph of Alumina-SPE; b) Photographs of a Flexed Alumina-SPE; c) SEM Image of Bare-SPE at 5,000X; d) SEM Image of Alumina-SPE at 5,000X; e) SEM Image of Bare-SPE at 50,000X; f) SEM Image of Alumina-SPE at 50,000X.

The ionic conductivity, σ , is one of the most crucial electrolyte properties for the Alumina-SPE and it was calculated using Eq. 4.1:

$$\sigma = \frac{L}{R_b S}, \quad \text{Eq. 4.1}$$

where L is the thickness of the membrane, S is its surface area, and R_b is its bulk resistance which is determined from the intersection between the real impedance axis and the Nyquist plot, displayed in Figure 4.2 a). The Alumina-SPE membrane demonstrates

an ionic conductivity of $1.32 \times 10^{-3} \text{ S} \cdot \text{cm}^{-1}$ at 24°C . This is a very high value for a solid-state polymer electrolyte and is comparable to that of a liquid electrolyte.^{5,7} The dependence of ionic conductivity on temperature was also analyzed, and an Arrhenius plot was generated, shown in Figure 4.2 b). As expected, the ionic conductivity increases with temperature, which is due to increased carrier mobility and faster segmental chain motion of the polymer. The ionic conductivity graph exhibits linear behavior, as opposed to Vogel-Tamman-Fulcher (VTF) trend.^{5,7} The Arrhenius model, shown in Eq. 4.2, demonstrates that the ions are transferred via solvent molecules rather than via polymer branches.^{5,7}

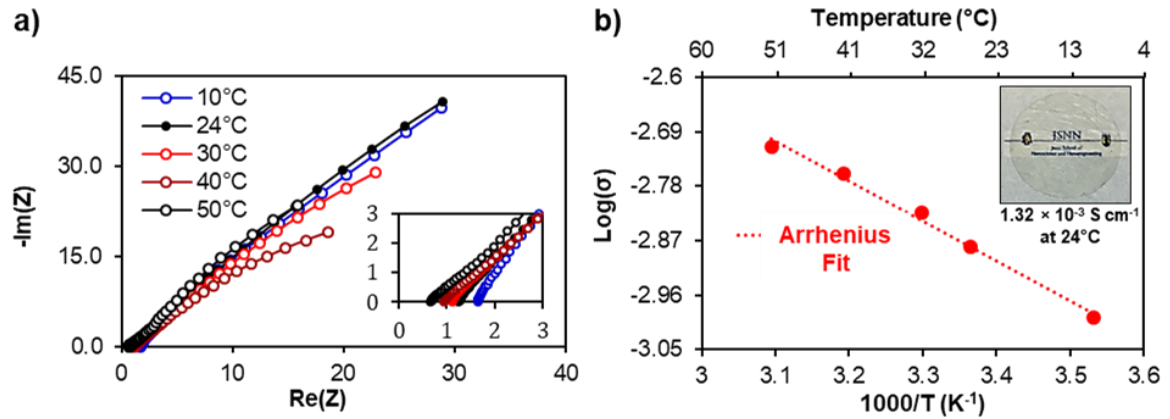


Figure 4.2. a) Nyquist Plots of Alumina-SPE; b) Temperature Dependence of Ionic Conductivity of Alumina-SPE.

$$\sigma = \sigma_0 \exp\left(\frac{E_a}{RT}\right) \quad \text{Eq. 4.2}$$

The Arrhenius equation was carried out to calculate the activation energy, E_a , which was found to equal to $1.67 \text{ kJ} \cdot \text{mol}^{-1}$. This value is low, and it is comparable to gel polymer

electrolytes based on nitriles.⁵⁻⁷ Most polymer electrolytes that can reach such high ionic conductivities and low activation energies are gel-based and transfer ions via a liquid electrolyte mechanism.⁵⁻⁶

In order to gain an insight into how the lithium ion is transferred within the SPE, Fourier Transform Infrared Spectroscopy (FTIR) was conducted, and the results are displayed in Figure 4.3. To track how glutaronitrile and polyacrylonitrile interact, there are four samples analyzed: LiPF₆/GN/EC, LiPF₆/PAN/EC, LiPF₆/GN/PAN/EC (bare-SPE), and LiPF₆/GN/PAN/EC/Al₂O₃ (Alumina-SPE). All of the samples display a small wide peak at 3600 cm⁻¹ which is attributed to an OH stretch due to a minuscule amount of moisture absorbed when the samples were exposed to air.⁸

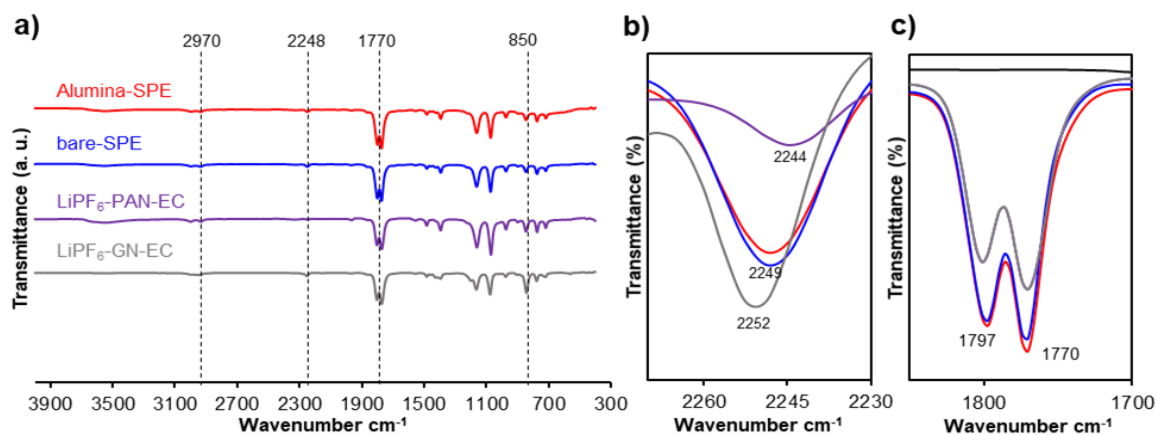


Figure 4.3. a) FTIR Results for LiPF₆-GN-EC, LiPF₆-PAN-EC, Bare-SPE, and Alumina-SPE; b) Enlarged Peak at ~2240 cm⁻¹ With the Sample Curves Overlapping to Emphasize Differences; c) Enlarged Peak at ~1770 cm⁻¹ With the Sample Curves Overlapping to Emphasize Differences.

The peak at 2970 cm⁻¹ corresponds to C-H stretching (gauche and trans), which stems from both glutaronitrile and polyacrylonitrile and therefore appears in all samples.⁵

The peak at 2240 cm^{-1} is paid special attention to because it corresponds to $\text{C}\equiv\text{N}$ stretching (gauche and trans).^{9,10} As can be seen from Figure 4.3 b), although some peak shifts are present, no shoulder peak appears in neither bare-SPE nor Alumina-SPE samples. The slight peak shifts can be attributed to the nitrile group interacting with the ions present in the sample.⁹⁻¹¹ However, the absence of the shoulder peak signifies that the nitrile group does not interact with the lithium ion.⁹⁻¹¹ This is an important finding because it means that the lithium ion bypasses the nitrile groups, and both polyacrylonitrile and glutaronitrile have little effect on the ionic conductivity. The most prominent peaks for all samples occur at 1797 and 1770 cm^{-1} , and they correspond to $\text{C}=\text{O}$ bond stretching due to the residual ethylene carbonate.¹² The high intensity of these peaks demonstrates that both bare-SPE and Alumina-SPE contain much solvent. Since the oxygen group on the $\text{C}=\text{O}$ bond is more electronegative than the nitrile group, the lithium ion is most likely interacting with ethylene carbonate rather than with PAN or GN. The high amount of ethylene carbonate remaining within the membranes is the cause behind their high ionic conductivity. The PAN in the system acts more like a mechanical stability filler for the EC-based gel electrolyte. Based on the FTIR results, the hypothesized lithium-ion conduction mechanism is an ethylene carbonate-based redox shuttle, which is the same mechanism present in liquid electrolytes. It appears that the polyacrylonitrile serves solely as a backbone, while glutaronitrile has no effect on the ionic transfer. Lastly, the peak at 850 cm^{-1} corresponds to the PF_6^- anion.¹³

Based on the amorphousness of the membranes, as demonstrated by the SEM results (Figure 4.1), the Arrhenius behavior derived from ionic conductivity plots (Figure

4.2) and high-intensity C=O peaks of SPE's FTIR spectra (Figure 4.3), it can be concluded that the lithium is transported via residual EC molecules within this SPE system, and not via the nitrile groups of glutaronitrile as originally hypothesized. The high amount of EC and its highly electronegative carbonyl group is high-jacking the lithium ions away from nitrile groups on GN and PAN. This reduces the role of glutaronitrile from an active ion transporter to a plasticizer. Since glutaronitrile remains liquid at room temperature, and the presence of LiPF₆ lowers the freezing point of ethylene carbonate, the excessive amount of liquid turns polyacrylonitrile into a soft amorphous gel.¹⁴ Therefore, PAN's only role within this electrolyte system is as a host for the active lithium ion conductor, which is ethylene carbonate. This shows that the high ionic conductivity of the system is solely due to the presence of a high amount of ethylene carbonate.

4.1.2 The Applicability of LiPF₆/GN/PAN/EC System

The applicability of the LiPF₆/GN/PAN/EC system within a battery is assessed in this section. In order to determine whether the SPE system is electrochemically stable enough to function within a battery, its voltage window was examined using LSV and CV; the results are shown in Figures 4.4 a) and b). Glutaronitrile is known for its cathodic stability and is often explored as a liquid electrolyte additive; therefore, a high electrochemical window is expected in its polymer electrolyte.^{15,16} It was found that both SPEs are stable up to 6V. However, after 3.5 V, the bare-SPE began to exhibit anodic current, similar to the liquid electrolyte-soaked polyethylene separator, which is most likely due to oxidation of ethylene carbonate. Nevertheless, it is important to note that the

current for bare-SPE is very low and is considered negligible.^{13,16} The Alumina-SPE displays no anodic current due to the alumina nanoparticles stabilizing the electrolyte. The CV of Alumina-SPE further proves the electrochemical stability of the Alumina-SPE within the 0 to 5 V range. This is well within the voltage window needed for successful battery operation.^{15,16}

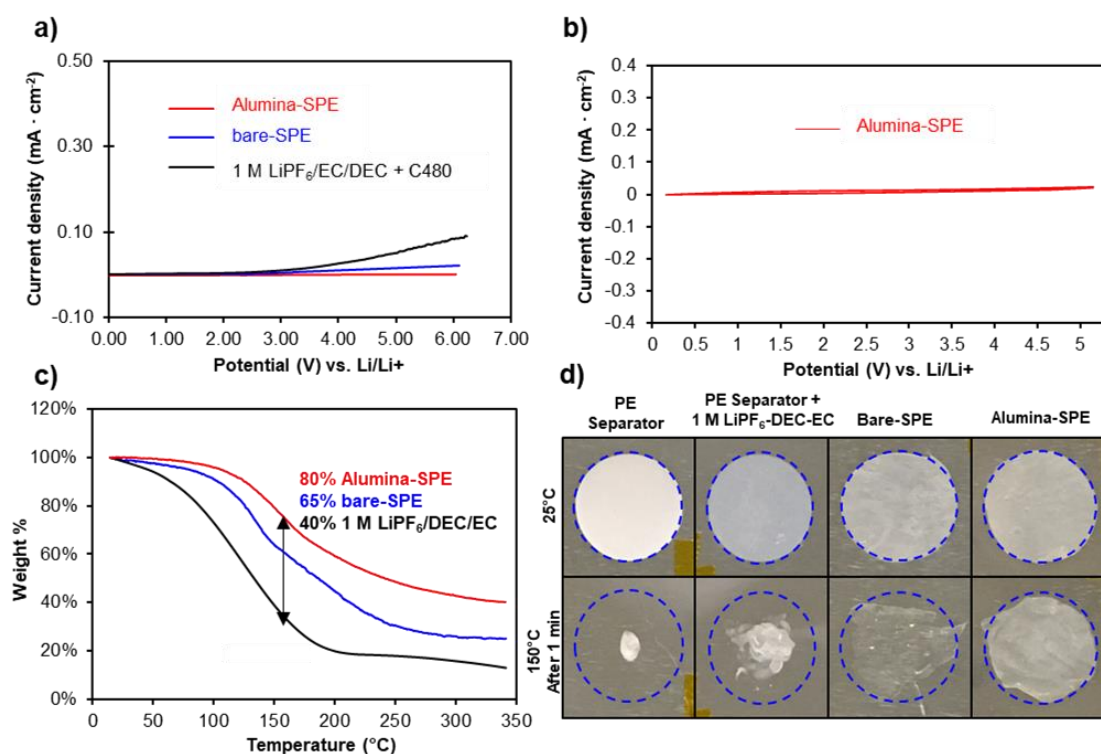


Figure 4.4. a) LSV Results of SPE Membranes Compared to Liquid Electrolyte (1 M LiPF₆-EC-DEC) Soaked Polyethylene Separator; b) CV Result of Alumina-SPE Membrane; c) TGA Results of SPE Membranes Compared to Liquid Electrolyte (1 M LiPF₆-EC-DEC) Soaked Polyethylene Separator; d) Photographs of the SPE Membranes and Polyethylene Separator With and Without Liquid Electrolyte (1 M LiPF₆-EC-DEC) at 25°C (Top Row) and 150°C (Bottom Row).

The safety of the LiPF₆/GN/PAN/EC system was also investigated since it is one of the major motivations behind solid electrolyte development. The safety was

investigated through thermal and mechanical analysis of the SPE membranes' properties. The thermal characteristics determine the susceptibility of catching fire during a short circuit, while the mechanical properties indicate SPE's ability to prevent short circuits caused by dendrites or foreign metallic particles.

The thermal properties of both SPE membranes were assessed using thermogravimetric analysis. The TGA results can be seen in Figure 4.4 c). The bare-SPE is negligibly volatile up to 115°C, while the Alumina-SPE is negligibly volatile up to 123°C. The increase in stability arises from the higher thermal integrity of Al₂O₃ nanoparticles. The loss in weight at those temperatures is most likely due to the remaining ethylene carbonate, which also confirms the high amount of ethylene carbonate within the samples. Both SPE membranes display higher stability compared to the liquid electrolyte (1 M LiPF₆-EC-DEC) soaked polyethylene (PE) separator, which lost 20% of its weight once it reached 80°C. The increased thermal stability can also stem from the presence of glutaronitrile which is thermally stable up to 267°C.¹¹ It is important to note, however, that the Alumina-SPE retained over 40% of its weight up to 350°C, which is a higher percentage than most SPEs of comparable ionic conductivities.^{15,17,18} In addition to TGA, we have also performed a heat test where bare-SPE, Alumina-SPE, polyethylene separator, and 1 M LiPF₆-EC-DEC polyethylene separator were placed onto a hot plate which was set to 150°C. As can be seen from Figure 4.4 d), both of the PE separators deformed after a minute of being placed onto a hot plate. The bare-SPE appears to have melted, most likely due to the residual EC. The Alumina-SPE maintained most of its original shape, its higher thermal stability arising from the alumina

nanoparticles. This test qualitatively demonstrates higher thermal integrity of the Alumina-SPE compared to the conventional separator. It shows that although there is a high amount of EC present, as discussed in Section 4.1.1, the thermal integrity and thereby safety of the SPE is improved compared to conventional liquid electrolyte/separator system.

For mechanical property characterization, tensile testing was conducted, and the results are displayed in Figure 4.5 a). The Young's modulus for SPE membranes was calculated via a 0.2% proof of strength method. This has resulted in a modulus of 0.8 MPa for Alumina-SPE and 0.41 MPa for bare-SPE. The increased value of the Alumina-SPE results from the mechanical integrity of Alumina nanoparticles. Although these results are below ideal, they still indicate that both of the SPEs possess some mechanical strength.³ The most likely cause of the reduced mechanical integrity is the presence of ethylene carbonate and glutaronitrile, which plasticize PAN, yielding more free volume within the polymer.³

To further demonstrate the safety of the Alumina-SPE membrane, we have conducted a nail penetration test with the results shown in Figure 4.5 b) – e). We have charged the all-state pouch cell to 4.047 V and drilled six fully penetrative holes, which resulted in an internal short circuit during the process. As can be seen from Figure 4.5 d) – e) the cell sustained its function and retained a potential difference of >3.9 V. For a liquid electrolyte pouch full cell, this type of experiment is dangerous as it can result in a fire due to the heat arising from the internal short circuit.

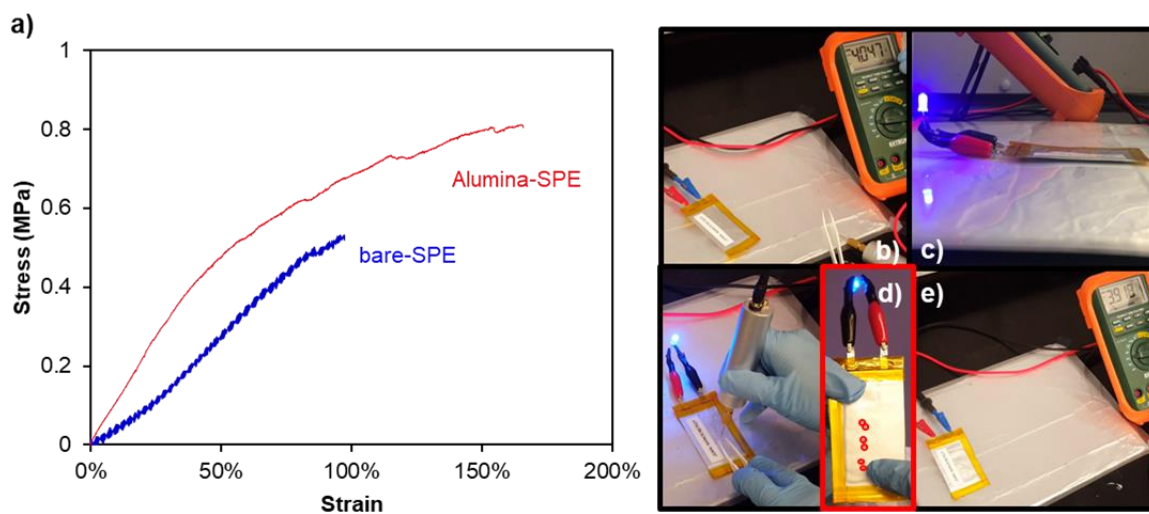


Figure 4.5. a) Tensile Testing Results of the Bare and Alumina SPE; b) Potential Difference of an All Solid NMC622/Graphite Pouch Cell Made With Alumina-SPE Membrane; c) Demonstration of an All Solid State Pouch NMC622/Graphite Cell Assembled With the Alumina-SPE as it Lights a Blue LED; d) Nail Penetration Test of the All Solid State Cell Depicted in b) and c) Which Results in Six Fully Penetrative Holes Which are Circled in Red; e) Demonstration of an All Solid State Pouch NMC622/Graphite Cell Assembled With the Alumina-SPE as it Retains >3.9 V After it Has Been Penetrated With a Drill.

The battery performance of the $\text{LiPF}_6/\text{GN}/\text{PAN}/\text{EC}$ system was also analyzed. We have assembled both coin and pouch full cells with $\text{LiNi}_{0.6}\text{Mn}_{0.2}\text{Co}_{0.2}\text{O}_2$ (NMC622) as the cathode and graphite as the anode. Both cells were cycled at 0.3C at 23°C. As can be seen in Figure 4.6 a), the pouch cell was able to achieve a formation cycle discharge capacity of 172.4 mAh/g with a Coulombic Efficiency of 80.1%, which is compared to the full cell assembled with a 1 M LiPF_6 -EC-DEC electrolyte and a polyethylene separator. As shown in Figure 4.6 b) - c), the pouch full cell was able to retain ~90% capacity retention after 100 cycles, while the coin full cell was able to attain a capacity retention of ~100% after 100 cycles. Figure 4.6 d) shows that the all-solid-state pouch cell can light up a white

LED light which requires at least 3.4 V to operate. These yield to be the most significant results of this study because it is rare for a polymer electrolyte to demonstrate full cell cycling at current rates above 0.1C at ambient temperature.^{3,15,17,18}

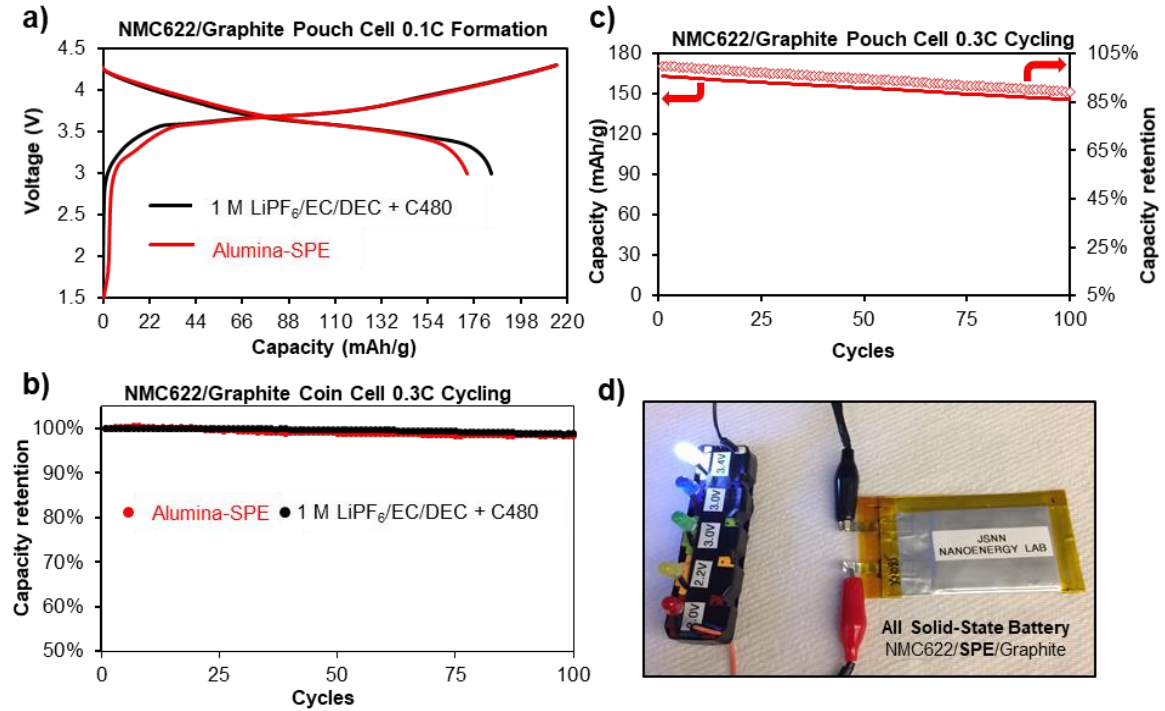


Figure 4.6. a) Voltage Profile During the Formation Cycle of the NMC622/Graphite Pouch Cells Performed at 23°C Using a Current Rate of 0.1C; b) Capacity Retention Graphs of the NMC622/Graphite Coin Cells Conducted at 23°C Using a Current Rate of 0.3C Which Results in a Current Density of 0.264 mA/cm²; c) Cycling of an All Solid State NMC622/Graphite Pouch Cell at 23°C Using a Current Rate of 0.3C Which Results in a Current Density of 0.268 mA/cm²; d) the All Solid State NMC622/Alumina-SPE/Graphite Pouch Cell Lighting a White LED (3.4V).

4.1.3 Concluding Remarks Regarding LiPF₆/GN/PAN/EC System

Overall, the Alumina-SPE achieved a high ionic conductivity of 1.32×10^{-3} S·cm⁻¹ at 24°C, which is comparable to liquid electrolyte values. Ionic conduction behavior is best described by the Arrhenius model, which indicates that the lithium ions

are transported by solvent molecules. The FTIR results demonstrate that the highly electronegative oxygen in the carbonyl group of ethylene carbonate steals lithium ions from the less electronegative nitrile groups. Therefore, neither PAN nor GN are participating in ion transport, and ion conduction occurs solely through ethylene carbonate molecules. The PAN in the system acts more like a mechanical stability filler for the EC-based gel electrolyte rather than an active participant in the ion conduction process. LSV and CV demonstrated that the Alumina-SPE is stable up to 6 V vs. Li/Li^+ , which is well within the operating range of the conventional battery. The high electrochemical stability of glutaronitrile is the reason for an improved functional voltage window. The Alumina-SPE is stable up to 123°C and is able to retain >40% of its weight at 350°C due to the high thermal stability of Alumina, PAN, and glutaronitrile. The full pouch cell containing the Alumina-SPE membrane retained ~90% of its capacity after 100 cycles at 0.3C and 23°C, which is a rare result for polymer electrolytes. The reason for such high performance is the amount of ethylene carbonate remaining within the electrolyte, which is also the main component within liquid electrolytes. Overall, the molecular glutaronitrile-based polymer electrolyte demonstrates very similar behavior to a conventional liquid electrolyte with the benefits of higher electrochemical and thermal stability due to the presence of GN, Alumina, and PAN.

This experiment neither confirms nor disproves the postulated hypothesis that the ion conduction mechanism of plastic crystal-based SPE occurs through lattice defects created due to conformational transformations in glutaronitrile. However, what this

study does show is that the lithium ion will surpass the nitrile groups in the presence of a carbonyl.

4.2 LiClO₄/GN/PAN System

This section addresses **Aim 1** of the study and discusses glutaronitrile's (GN's) role in ion conduction within the first SPE system comprising of lithium perchlorate (LiClO₄) as the lithium salt and polyacrylonitrile (PAN) as the mechanical backbone. Additionally, all of the ethylene carbonate has been removed from this system. Experimental procedures pertaining to this section are described in 3.2.1 – 3.2.3.

4.2.1 Interaction Between Li⁺ Ions and Glutaronitrile

Figure 4.7 a) shows the FTIR spectra of GN and the LiClO₄/GN system at room temperature. The spectra for all of the samples are very similar; however, there are a few differences. One of the differences is a peak at 2248.6 cm⁻¹ that represents the unbound nitrile group as displayed in Figure 4.7 b).⁶ There is another peak emerging at 2275 cm⁻¹ which corresponds to the bound nitrile group.⁶ As has been demonstrated by previous studies, this latter peak represents the nitrile group interacting with lithium. It can be seen that the concentration of LiClO₄ does not affect these peaks. This means that about the same amount of lithium-bound nitrile groups exist regardless of the concentration at room temperature. It is important to note that at room temperature, concentrations higher than 3mol% mmol begin to crystallize due to the supersaturation of the solution. This aspect can therefore affect the concentration of dissolved lithium in the solution, thereby changing the concentration of each sample.

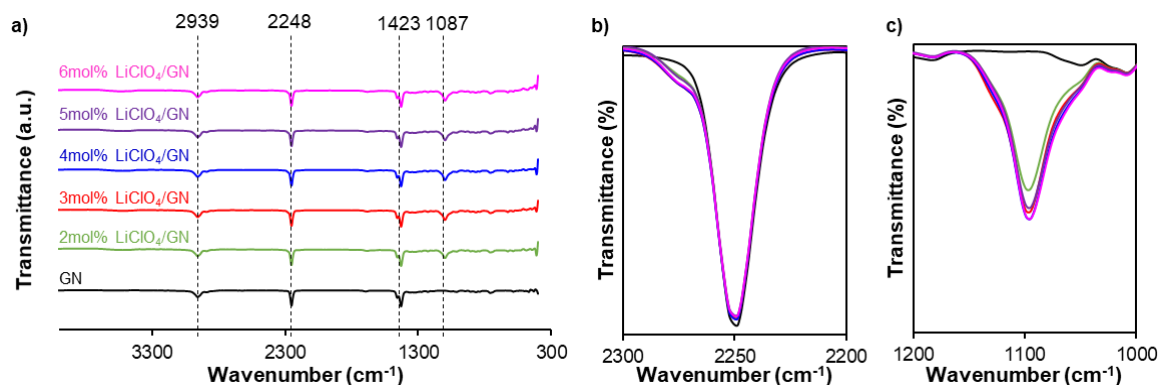


Figure 4.7. FTIR Spectra of GN and the LiClO₄/GN System at 23°C. a) Overall Spectra; b) Nitrile Peaks; c) ClO₄⁻¹ Anion Peak.

Another difference is the peak at 1095 cm⁻¹ which corresponds to the ClO₄⁻¹ anion.¹⁹ It is demonstrated in Figure 4.7 c) that this peak is higher for higher concentrations. However, for 3mol% – 6mol% concentrations, the intensity differences are negligible, most likely due to the recrystallization of LiClO₄.

Figure 4.8 a) displays the FTIR spectra of GN and the LiClO₄/GN system at 80°C. Unlike in the room temperature spectra, the nitrile bound peak at 2275 cm⁻¹ becomes more pronounced, and the concentration effect is now apparent – as the concentration increases, so does this peak's intensity.²¹ Moreover, the unbound peak at 2248.6 cm⁻¹ experiences a slight loss in intensity as the concentration increases.^{20,21} This suggests that the number of bound nitrile groups increases with concentration, while the number of unbound nitrile groups decreases. The reason this effect was not seen in the room temperature spectra is due to the recrystallization of LiClO₄. At 80°C, there are more dissolved lithium ions, thereby increasing the chance of them binding to GN's nitrile group.

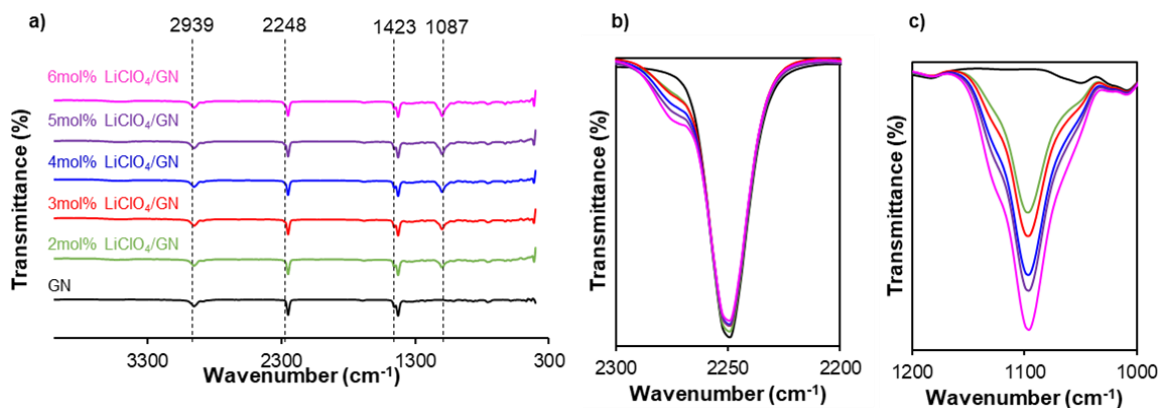


Figure 4.8. FTIR Spectra of GN and the LiClO₄/GN System at 80°C. a) Overall Spectra; b) Nitrile Peaks; c) ClO₄⁻¹ Anion Peak.

The peak at 1095 cm⁻¹, corresponding to the ClO₄⁻¹ anion,²² also increases with concentration which suggests that as the concentration rises, the number of ClO₄⁻¹ anions also increases.

It is also important to consider how temperature and the lithium-ion concentration affect GN's conformation. Some studies argue that the gauche is the most abundant conformation in nitrile plastic crystals due to there being two gauche configurations and only one trans configuration.^{22,23} However, it is important to consider that trans is more energetically favorable. And as the lithium ion binds to one of the nitrile groups, it is less likely to enter a gauche conformation due to the increase in the bulkiness of the molecule. Nevertheless, because the solution is in a liquid phase, its molecules are constantly rotating; therefore, there are different amounts of each conformation at any given moment. This aspect complicates the identification of GN's most likely conformation.

4.2.2 Interaction Between Li⁺ Ions and Glutaronitrile Within a Polymer

Lithium ion's interaction with nitrile groups within a polymer was also analyzed, as shown in Figure 4.9. Figure 4.9 a) demonstrates an overall FTIR spectrum, and Figure 4.9 b) shows the nitrile peak at 2250 cm⁻¹.⁶ A small shoulder peak at 2275 cm⁻¹, which corresponds to the nitrile group interacting with the lithium ion, is evident. Moreover, the shoulder peak increases as salt concentration increases, which is due to the increase in charge carriers.^{6,24} Figure 4.9 c) shows the carbonyl peak corresponding to the ethylene carbonate solvent. In the LiPF₆/GN/PAN/EC system, the ethylene carbonate remained in the SPE after drying and therefore hijacked the lithium ions away from the nitrile groups of GN and PAN. However, due to the better drying procedure, the amount of ethylene carbonate was reduced, allowing for lithium ions to interact with the nitrile groups. Lastly, Figure 4.9 d) represents the peak 1650 cm⁻¹, which corresponds to the ClO₄⁻¹ anion.^{20,25}

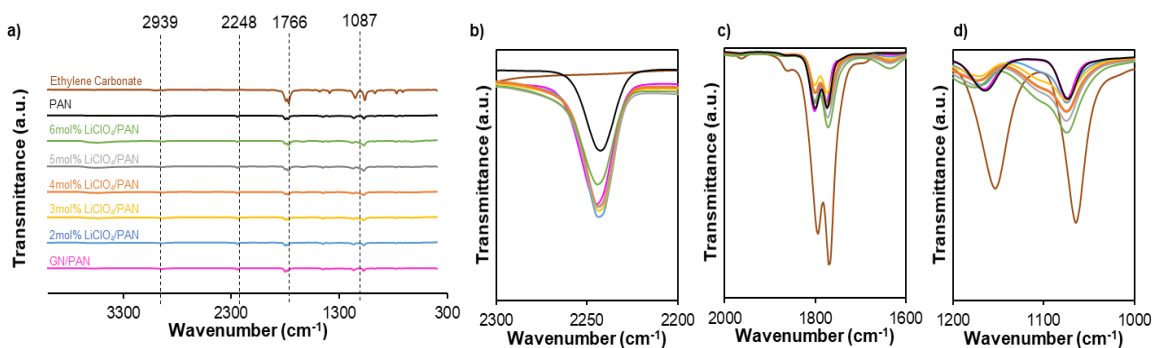


Figure 4.9. FTIR Spectra of LiClO₄/PAN System at 23°C. a) Overall Spectra; b) Nitrile Peaks; c) Carbonyl Peaks; d) ClO₄⁻¹ Anion Peak.

The FTIR spectra of the addition of glutaronitrile to the LiClO₄/PAN system are shown in Figure 4.10. As can be seen from 4.10 b), the addition of glutaronitrile results in increased interaction between lithium and the nitrile group due to the increase in the 2275 cm⁻¹ shoulder peak.⁶ It should be noted that the salt concentration is correlated with the lithium ion interaction, which is also reflected in the LiClO₄ peaks in Figure 4.10 c). Additionally, the carbonyl peaks for most samples are slightly lower than for the LiClO₄/PAN samples, which can also lead to the increase Li⁺ interaction with the nitriles.

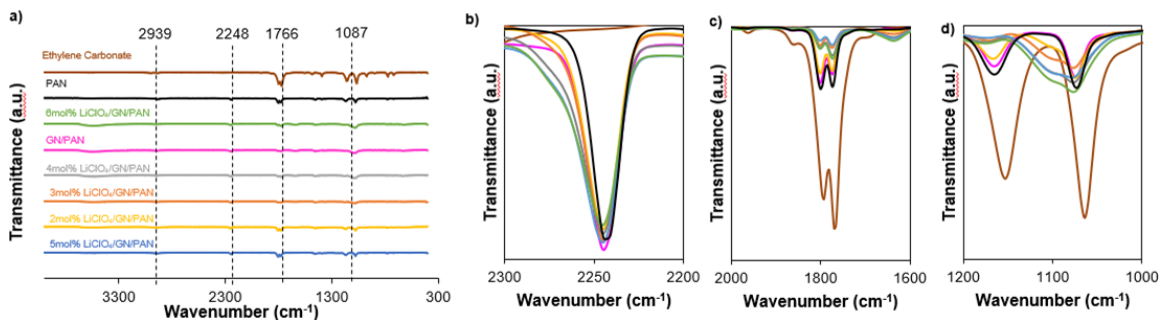


Figure 4.10. FTIR Spectra of GN and the LiClO₄/GN/PAN System at 23°C. a) Overall Spectra; b) Nitrile Peaks; c) Carbonyl Peaks; d) ClO₄⁻ Anion Peak.

Ionic conductivity of both LiClO₄/PAN and LiClO₄/GN/PAN systems was also measured, and the results are shown in Figure 4.11 and Table 4.1. The ionic conductivities were calculated as described in Section 2.3. As has been demonstrated by Ahmad *et al.*, PAN was not ionically conductive and was therefore omitted from Figure 4.11.²⁹ An increase in ionic conductivity with higher salt concentration can be seen due to the decrease in the Nyquist plot size and shift towards lower real impedance values.^{27,28} The increase in ionic conductivity with higher salt concentration occurs due to the rise in charge carriers and due to the lowering of PAN's glass transition temperature.^{4,5} The

latter allows more free space for polymer chain movement, which aids faster ion transfer.^{4,5}

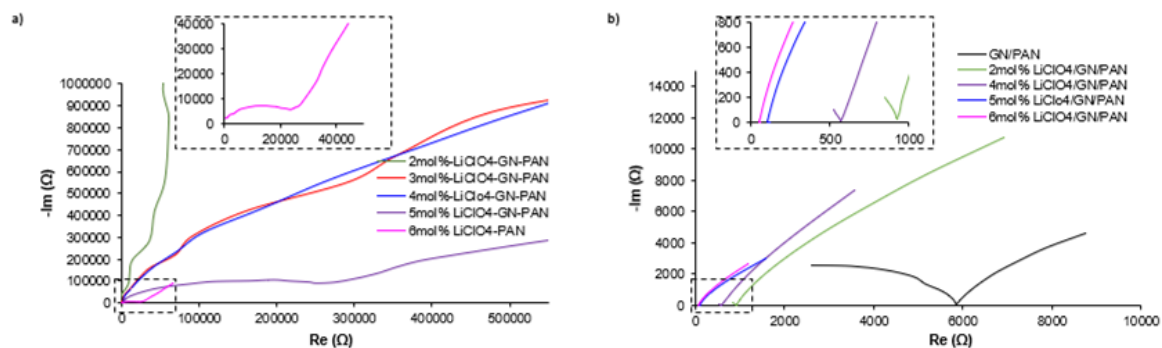


Figure 4.11. a) Nyquist Plots of the LiClO₄/PAN System at 24°C; b) Nyquist Plot of the LiClO₄/GN/PAN System at 24°C.

As can be seen in Figure 4.11 b), the Nyquist plot sizes of the LiClO₄/GN/PAN system are drastically smaller and are shifted towards the lower real impedance values. This indicates that the addition of glutaronitrile improves ionic conductivity for all salt concentrations. This can also be deduced from ionic conductivities displayed in Table 4.1, which shows a substantial increase with the addition of GN. However, it should be noted that the addition of GN reduces the glass transition temperature of polyacrylonitrile.⁴ The allowance for more free space increases PAN polymer chain movement, which yields faster ion transfer.^{4,5} Therefore, it is unclear whether the increase in ionic conductivity is due to glutaronitrile promoting lithium ion interaction with the nitrile groups or due to GN functioning as the plasticizer. It is also observed that the GN/PAN sample possesses some ionic conductivity despite the lack of Li⁺ charge carriers. The small amount of ion transfer can be stemming from ions originating from

the copper electrodes and H^+ ions from any trapped moisture in the samples. The rise in ionic conductivity with the addition of GN in the GN/PAN sample can be due to the same reasons as in the Li^+ ion case.

Mol%	No GN - IC (S/cm ²)	With GN - IC (S/cm ²)
0	N/A	1.16×10^{-5}
2	8.59×10^{-6}	2.22×10^{-5}
3	1.75×10^{-5}	7.92×10^{-5}
4	2.22×10^{-5}	1.05×10^{-4}
5	2.92×10^{-5}	1.06×10^{-4}
6	3.44×10^{-5}	1.73×10^{-4}

Table 4.1. Calculated Ionic Conductivities of $LiClO_4$ /PAN (No GN) and $LiClO_4$ /GN/PAN (With GN) Systems at 24°C.

The highest ionic conductivity that was reached is $1.73 \times 10^{-4} \text{ S}\cdot\text{cm}^{-1}$ at 24°C for 6mol% $LiClO_4$ /GN/PAN. This is one magnitude lower than the ionic conductivity of the $LiPF_6$ /GN/PAN/EC system. This difference can originate from several aspects. One of the major aspects is the higher SPE plasticity of the EC system. Because EC lowers PAN's glass transition temperature more than GN alone, the increase in polymer chain movement can dramatically improve conduction.^{4,5} Moreover, as Sai *et al.* discuss, Li^+ ions are more likely to coordinate with oxygen due to oxygen's higher electron affinity compared to nitrogen.²⁵

The electrical conductance of the $LiClO_4$ /GN/PAN system was also assessed, and the IV plots are shown in Figure 4.12, while conductivity values, calculated as described in Section 3.2.3, are displayed in Table 4.1. Considering that these systems are designed

to be used for a battery separator application, it is expected to have low electrical conductivity. The addition of LiClO_4 has enhanced the electrical conductance due to the current being carried by the Li^+ and ClO_4^{-1} ions.²⁹ The addition of GN to PAN increased the electrical conductance, which can be attributed to several factors. There can be ions present in the system either from traces of ionizable impurities of precursor materials or from moisture. Similar to the ionic conductivity measurement, the glutaronitrile acting as a plasticizer can increase electrical conductivity by enabling ion transfer, thus giving rise to a higher current. It is important to note that the flow of current is stemming from the ions rather than electrons since PAN is electrically a non-conductive polymer.²⁹ Therefore, the increase in conductance observed in the $\text{LiClO}_4/\text{GN}/\text{PAN}$ and $\text{LiClO}_4/\text{PAN}$ samples are due to the addition of the lithium salt. There was no trend observed when increasing the salt concentration from 3mol% to 6mol%. The higher conductance of the 3mol% $\text{LiClO}_4/\text{GN}/\text{PAN}$ sample can be due to higher moisture content and thus an increased H^+ concentration.

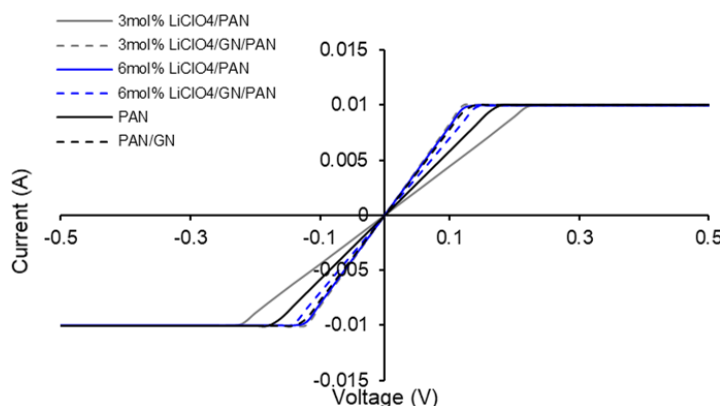


Figure 4.12. IV Plots of the $\text{LiClO}_4/\text{PAN}$ and $\text{LiClO}_4/\text{GN}/\text{PAN}$ Systems.

Sample	G (mS)
PAN	18
PAN/GN	22.3
3mol% LiClO ₄ /GN/PAN	24.6
6mol% LiClO ₄ /PAN	24.1
6mol% LiClO ₄ /GN/PAN	21.5

Table 4.2 Calculated Electrical Conductance Values of LiClO₄/PAN and LiClO₄/GN/PAN Systems.

4.2.3 Concluding Remarks Regarding LiClO₄/GN/PAN System

The shoulder peak at 2270 cm⁻¹ can be easily visible for the LiClO₄/GN solutions measured at 80°C samples. This demonstrates that the lithium ion can coordinate with GN's nitrile group. The presence of this peak in this system, and its absence in the LiPF₆/GN/PAN/EC system, further proves that the main ion conduction mechanism in the EC-based system is the redox shuttle through ethylene carbonate's oxygen groups. It was also demonstrated that the salt concentration has a direct effect on the height of the peak, with the higher concentration allowing for more charge carriers to interact with the GN molecule. The improved drying procedure of the SPE helped reduce ethylene carbonate content and allow for lithium ions to interact with the nitrile groups. The peak at 2270 cm⁻¹ was also present in this system, which displays that major ion transfer was occurring through the nitrile groups. However, the highest ionic conductivity achieved was $1.73 \times 10^{-4} \text{ S} \cdot \text{cm}^{-1}$ at 24°C, an order of magnitude lower than the LiPF₆/GN/PAN/EC system. This displays that the lithium ion transfer occurs more rapidly through the ethylene carbonate groups. The electrical conductance was also investigated, and it was

shown that the systems have low electrical conductance value; however, the addition of LiClO₄ increased the flow of current due to the rise in charge carriers. *This experiment shows that the lithium ion can transfer via glutaronitrile's nitrile groups; however, this ion transfer is much slower than the ethylene carbonate redox shuttle, which is the main ion conduction mechanism in the LiPF₆/GN/PAN/EC system.*

4.3 Zn MOF as Ion Conductors

This section explores Zn MOF's potential as an ion conductor—by itself and with additives. Metal-organic frameworks are a common filler used within polymer electrolytes; however, their applicability as a solid electrolyte remains unclear.³¹

4.3.1 Zn MOF Ionic Conductivity

Zn MOFs were synthesized as described in Section 3.3.1, and as in Dawood *et al.*³² Zn MOF morphology was analyzed to ensure successful synthesis using FE-SEM. As can be seen from Figure 4.13, and as revealed in Dawood *et al.*, Zn MOF particles display truncated hexagonal and irregularly shaped microstructures.³² As per Dawood *et al.*, Zn MOF are crystalline, have an optical band gap of 2.84 eV, which is indicative of semiconducting properties, and its thin films of microstructures exhibit an electrical conductivity of $3.98 \times 10^{-2} \text{ S}\cdot\text{cm}^{-1}$ at room temperature.³²

In order to investigate ion diffusion within Zn MOFs, its ionic conductivity was measured using EIS, as described in Section 3.2. The MOF powder was condensed into a pellet (0.0897 cm thickness, 19 mm diameter), shown in the inset of Figure 4.13 b), as discussed in Section 3.3. The Zn MOF pellet displayed open circuit behavior which indicates insulator properties. As discussed in Dawood *et al.*, Zn MOF thin films have an

electrical conductivity of 3.98×10^{-2} to $2.16 \times 10^{-2} \text{ S}\cdot\text{cm}^{-1}$ due to its loosely bound electrons around the metal ions and due to its extended hierarchical structures formed by metal ions and coordinating atoms of the ligands.³² The reason for a loss in electrical conductivity stems from the method of measurement. The pellet is formed by pressing the loose MOF powder together rather than allowing the formation of the interpenetrated networks, as in the case of the thin films. Therefore, the lack of defined conduction pathways prevents both electrons and ions from traveling through the pellet. Moreover, thin films reduce the impedance between the sample and electrodes due to a higher contact surface area, while the presence of more air gaps between the electrodes and the pellet decreases its ionic conductivity.^{33,34} For these reasons, the Zn MOF pellet displays neither electrical nor ionic conductivity in their Nyquist plots.

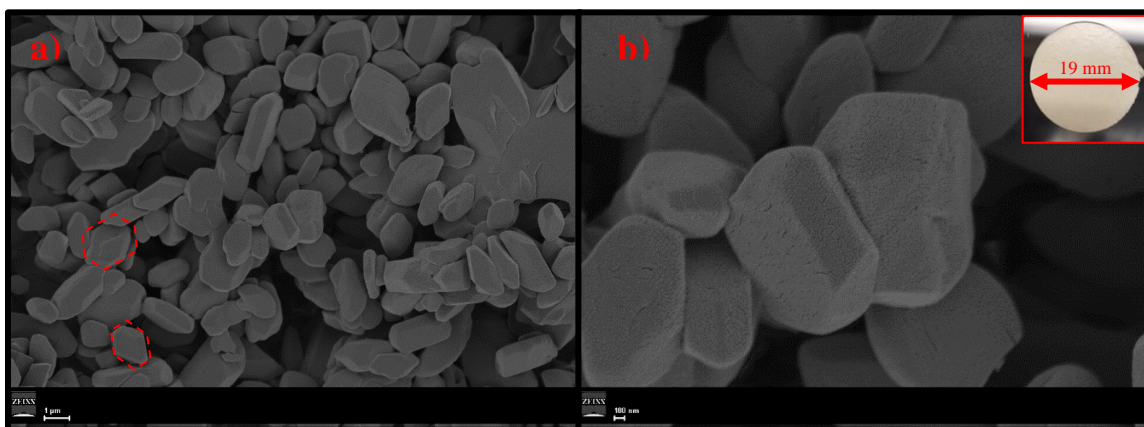


Figure 4.13. SEM Images of Zn MOF. The Red Dashed Lines Outline the Hexagonal Shape. a) Magnification of 5,000X and b) 20,000X. The Insert Shows the Zn MOF Pellet.

4.3.2 Improving Ionic Conductivity of Zn MOF Using Electrolytic Solutions

It is hypothesized that Zn MOF is not ionically conductive because it does not contain enough free charge carriers to conduct current. To improve the ion conductivity of Zn MOFs, different electrolytic solutions were used to introduce ions into the Zn MOF system, as described in Section 3.3.3. Therefore, a 10 μL drop of deionized water was dropped and soaked into the pellet, after which an EIS measurement was performed as described in Section 3.2. The results can be seen in Figure 4.14 a).

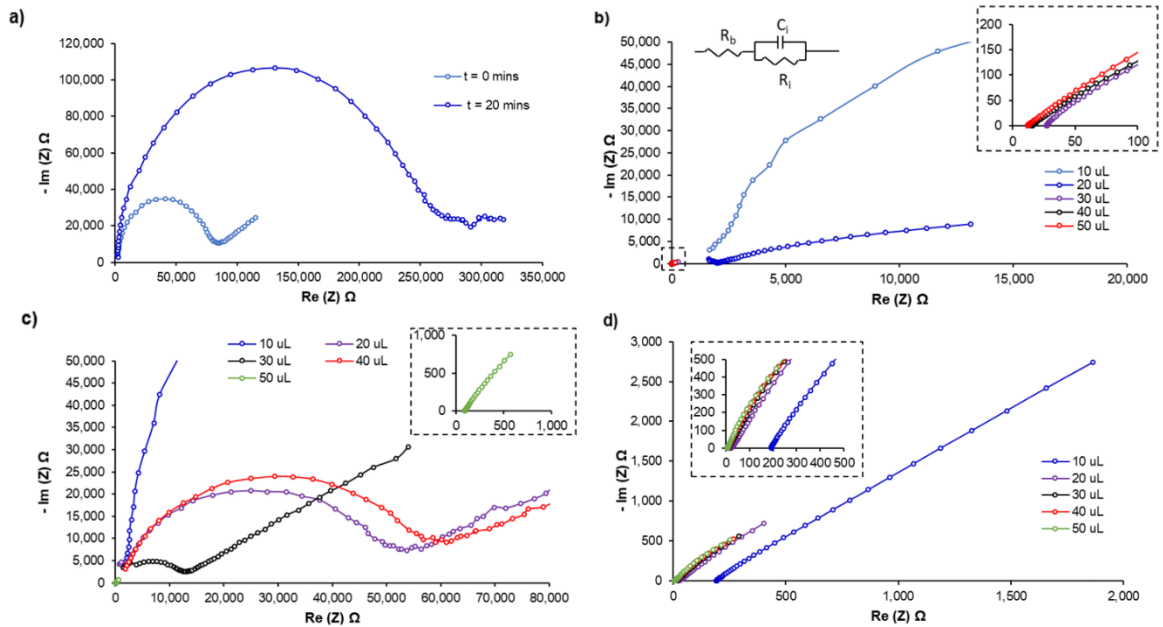


Figure 4.14. Nyquist Plots of Zn MOF Pellet With of a) 10 μL of Deionized Water at Measurement and After 20 Minutes, b) Various Amounts of 10wt% $\text{LiClO}_4/\text{DMF}$ Solution, c) Various Amounts of 10wt% $\text{LiClO}_4/\text{TMF}$ Solution and d) Various Amounts of 10wt% LiClO_4/GN . The Circuit Model Used to Calculate the Ionic Conductivity is Represented as an Inlet b).

The water contains protons, which transfer the charges through the pellet.

Considering that the Nyquist plot size increases after 20 minutes, it can be deduced that

as the water evaporates from the pellet, its resistance increases. Although the ionic conductivity increased with the addition of deionized water, it is unclear whether the protons are transferred through the framework or if they are transferred via solvent molecules.

To test this further, 50 μL of 10wt% $\text{LiClO}_4/\text{THF}$ solution was drop cast onto the pellet, and the Zn MOF pellet was then dried for one hour in a vacuum at room temperature to allow the THF to evaporate fully, after which another EIS measurement was taken. Lithium perchlorate is soluble in THF; therefore, the Zn MOF pellet would be enriched with both Li^+ and ClO_4^{-1} ions.³⁵ The pellet displayed open circuit behavior similar to Zn MOF alone, despite the Li^+ and ClO_4^{-1} remaining within its framework. The charges are therefore transferred via the solvating ClO_4^{-1} anion, alike to the proton conduction described by the Grotthuss mechanism in Meng *et al.* or via the redox shuttle created by the THF molecules.^{37,39,40} As in the case of the ethylene carbonate redox shuttle, the THF redox shuttle contained four THF molecules, with their oxygen groups interacting with one lithium ion.⁴⁰ Considering the drastic reduction in conductivity, the Zn MOF framework alone is not suitable to transfer charges and functions more as a host rather than an active ion conductor. The later discussions explore Zn MOF's potential as a mechanically stable host for electrolytic solutions.

The next experiment involved an electrolytic solution comprised of 10wt% $\text{LiClO}_4/\text{DMF}$. The solution was drop cast onto the pellet in 10 μL installments; after each drop, the ionic conductivity was measured as described in Sections 3.2 and 3.3.3. Lithium perchlorate is soluble in DMF; therefore, the Zn MOF pellet would be supplemented with

both Li^+ and ClO_4^{-1} ions.³⁵ The resulting Nyquist plots can be seen in Figure 4.14 a). It is evident that as the amount of the 10wt% $\text{LiClO}_4/\text{DMF}$ increased, the bulk resistance decreased, thereby improving ionic conductivity, as demonstrated in Table 4.3. However, it should be noted that this solution was dissolving the pellet. This was occurring due to DMF destroying the linkers within the framework.^{36,37} At 30 μL , the cracks of the pellet began to be filled with solvent, thereby degrading Zn MOF's ability to be a mechanically stable host. As mentioned above, the ions are being transferred via the DMF molecule redox shuttle or the ClO_4^{-1} -based Grotthuss mechanism. Similar to THF, the redox shuttle consists of four DMF molecules with the oxygen groups interacting with the lithium ion.⁴⁰

Solution volume	Zn MOF + $\text{LiClO}_4/\text{THF}$ σ ($\text{S}\cdot\text{cm}^{-1}$)	Zn MOF + $\text{LiClO}_4/\text{DMF}$ σ ($\text{S}\cdot\text{cm}^{-1}$)	Zn MOF + LiClO_4/GN σ ($\text{S}\cdot\text{cm}^{-1}$)
0 μL	Open Circuit	Open Circuit	Open Circuit
10 μL	1.60×10^{-5}	1.46×10^{-5}	5.20×10^{-5}
20 μL	4.47×10^{-5}	9.94×10^{-4}	5.13×10^{-4}
30 μL	1.52×10^{-4}	1.76×10^{-3}	1.10×10^{-3}
40 μL	2.00×10^{-5}	1.98×10^{-3}	1.72×10^{-3}
50 μL	2.07×10^{-4}	2.27×10^{-3}	1.68×10^{-3}

Table 4.3. Ionic conductivity results of Zn MOF pellet with added 10wtl% $\text{LiClO}_4/\text{THF}$, 10wt% $\text{LiClO}_4/\text{DMF}$, and 6wt% LiClO_4/GN .

A solution composed of 10wt% $\text{LiClO}_4/\text{THF}$ was applied in the same manner to the Zn MOF pellet as described in Section 3.3.3. The pellet was quickly absorbing the solution instead of being dissolved, unlike the case utilizing the DMF-based solution. The

resulting Nyquist plots are shown in Figure 4.13 b). The overall trend shows that the increase of solution reduces the bulk resistance. The rise in the ionic conductivity of Zn MOF with the addition of the 10wt% $\text{LiClO}_4/\text{THF}$ can be explained by the solution being encapsulated within the framework of the material. The higher amount of solution equates to the higher number of charges available for transfer. Additionally, the higher amount of solvent results in a higher amount of THF molecules transferring ions through the redox shuttle, as discussed above.^{37,40} The ionic conductivities at each solution amount can be seen in Table 4.3. The EIS behavior at 40 μL needs to be acknowledged because the bulk resistance at this concentration is significantly higher than the bulk resistance for 20 and 30 μL . A possible explanation for this phenomenon could be that the solution did not fully penetrate the pellet prior to the measurement.

The last solution evaluated was 6wt% LiClO_4/GN . Nyquist plots are shown in Figure 4.14 d), and ionic conductivity is displayed in Table 4.3. It should be noted that its salt concentration is lower than the previously discussed solutions. This is due to a solubility threshold being reached at 6wt% at room temperature and the solution being saturated above 6wt%. It was observed that GN did not dissolve the pellet, unlike in the DMF-based electrolytic solution; rather, the solution was absorbed by the pellet. A similar trend as with other solutions can be seen with the increase in solution amount leading to a rise in ionic conductivity. As with the previous solutions, this is explained by the increased number of ions and solvent molecules as the solution amount within the pellet increases.^{37,39,40}

It is observed that 6wt% LiClO₄/GN solution achieved the highest ionic conductivity, with $1.68 \times 10^{-3} \text{ S}\cdot\text{cm}^{-1}$ at 50 μL , while 10wt% LiClO₄/THF resulted in the lowest ionic conductivity with $2.07 \times 10^{-4} \text{ S}\cdot\text{cm}^{-1}$ at 50 μL . DMF will be emitted from these comparisons due to it dissolving the pellet and degrading its mechanical stability. There are several factors that influence the ionic conductivity of the Zn MOF/electrolytic solution system: 1) solution viscosity, 2) the number of free charges, 3) solvent molecules' ability to conduct ions, and 4) solvent molecules' ability to travel through the framework during ion transfer. The correlation between ionic conductivity and solvent viscosity is well studied in liquid electrolytes.^{41,42} Ion conduction in liquid electrolytes follows Arrhenius behavior and thereby depends upon ionic mobility, which decreases as the fluidity of the solvent is reduced.⁴² The viscosity of THF is 0.48 cP, which is much lower than glutaronitrile's viscosity of about 20 cP.^{43,44} Considering GN's higher ionic conductivity, even at a higher viscosity, the other factors are playing a more crucial role. The second factor considered is the number of free charges. As discussed above, the glutaronitrile-based solution contains a lower concentration of LiClO₄ due to solubility compared to the THF solution. Therefore, the 10wt% LiClO₄⁻¹/THF contains a higher number of free charges; however, it still has lower ionic conductivity. The next factor considered involves the solvent molecules' ability to conduct charges. The oxygen on the tetrahydrofuran has a higher electronegativity compared to GN's nitrogen group, which yields to higher interaction with the lithium ion, as discussed in Sections 4.2.1 and 4.2.2.²⁵ This leaves only one factor to contribute to GN's higher ionic conductivity, which is glutaronitrile's ability to maneuver through the Zn MOF framework while

coordinated to the lithium ion. Both THF and GN are similar in size (6.6 Å molecular diameter⁴⁵ versus 6.8 Å molecular diameter,⁴⁶ respectively). Therefore, solvation structure size is the crucial difference in molecule maneuverability. Shen *et al.* discuss the succinonitrile (SN) solvation structure with the lithium ion.²² Using the rotation decay time constant, they deduce that the likeliest coordinate number of SN molecules at room temperature to one lithium ion is two.²² They also calculate potential solvation structures between two SN molecules and one lithium ion using density functional theory (DFT) calculation. From the calculations, they infer that two of the solvation structures have the highest probability, and both of those structures involve three nitrile groups interacting with one lithium ion.²² Considering the similarity between the molecules, it can be assumed that the solvation structure of glutaronitrile would be similar to that of succinonitrile. Jarek *et al.* show that THF coordinates with four lithium ions which increases its solvation structure size.⁴⁷ Therefore, it can be concluded that mobility is a key factor that allows GN to yield higher ionic conductivity within the MOF system.

5.3 Conclusion

Several conclusions can be drawn from the reported observations. First of all, pure Zn MOF material is not ionically conductive, most likely due to the absence of charge carriers. Secondly, the ionic conductivity of the Zn MOF can be easily increased with the introduction of a salt solution.⁵⁻⁷ In this study, a 10wt% LiClO₄/THF showed the best results because it did not dissolve the pellet; rather, it was absorbed, and the ionic conductivity was drastically improved with the addition of this solution. One of the possible explanations for this phenomenon is that this solution is being encapsulated by

the organic framework and that the lithium ion is being solvated by the ClO_4^- anion within trapped THF similar to the Grotthuss mechanism.⁸

5.4 References

1. H K Koduru *et al.* Synergetic effect of TiO₂ nano filler additives on conductivity and dielectric properties of PEO/PVP nanocomposite electrolytes for electrochemical cell applications. *J. Phys.: Conf. Ser.* **780**, 012006 (2017).
2. Y.L. Yap, A.H. You, L.L. Teo, H. Hanapei. Inorganic Filler Sizes Effect on Ionic Conductivity in Polyethylene Oxide (PEO) Composite Polymer Electrolyte, *Int. J. Electrochem. Sci.* **8**, 2154 – 2163 (2013).
3. Liping Yue, Jun Ma, Jianjun Zhang, Jingwen Zhao, Shanmu Dong, Zhihong Liu, Guanglei Cui, Liquan Chen, All-solid-state polymer electrolytes for high-performance lithium ion batteries, *Energy Storage Materials*, **5**, 139–164 (2016).
4. Mindemark, J., Lacey, M. J., Bowden, T. & Brandell, D. Beyond PEO—Alternative host materials for Li⁺-conducting solid polymer electrolytes. *Prog. Polym. Sci.* **81**, 114–143 (2018).
5. Li-Zhen Fan, Ziao-Liang Wang, Fei Long. All-solid-state polymer electrolyte with plastic crystal materials for rechargeable lithium-ion battery, *Journal of Power Sources*, **180**, 775-778 (2009).
6. Manesh Zachariah *et al.*, Self-Diffusion. Phase Behavior, and Li⁺ Ion Conduction in Succinonitrile-Based Plastic Cocrystals, *J. Phys. Chem. C*, **119**, 27298–27306 (2015).
7. H. Lawrence Clever, Claw A. Wulff, and Edgar F. Westrum, Jr, Glutaronitrile. Calorimetrically Determined Thermal Properties from 5 to 350°K, and Statistical Gaseous Entropy. *J. Phys. Chem.* **69**, (1965).
8. Abu-Lebdeh, Y. & Davidson, I. New electrolytes based on glutaronitrile for high energy/power Li-ion batteries. *J. Power Sources* **189**, 576–579 (2009).
9. Liyu Jin, Patrick C. Howlett, Jennifer M. Pringle, Judith Janikowski, Michel Armand, Douglas R. MacFarlane and Maria Forsyth. An organic ionic plastic crystal electrolyte for rate capability and stability of ambient temperature lithium batteries, *Energy Environ. Sci.* **7**, 3352-3360 (2014).
10. Doron Aurbach, “Nonaqueous Electrochemistry,” CRC Press, (1999).

11. Zachariah, M., Romanini, M., Tripathi, P., Tamarit, J. L. & Macovez, R. Molecular diffusion and dc conductivity perfectly correlated with molecular rotational dynamics in a plastic crystalline electrolyte. *Phys. Chem. Chem. Phys.* **17**, 16053–16057 (2015).
12. Jianhua Fang, Jinli Qiao, David P. Wilkinson, Jiuju Zhang, Electrochemical Polymer Electrolyte Membranes, *Electrochemical Storage and Conversion*, CRC Press, (2015).
13. Choi, N.-S. et al. Degradation of spinel lithium manganese oxides by low oxidation durability of LiPF₆-based electrolyte at 60°C. *Solid State Ionics* **219**, 41–48 (2012).
14. Alarco, P.-J.; Abu-Lebdeh, Y.; Abouimrane, A.; Armand, M. The Plastic-Crystalline Phase of Succinonitrile as a Universal Matrix for Solid-State Ionic Conductors. *Nat. Mater.* **3** (7), 476–481 (2004).
15. Pu Hu, Jingchao Chai, Yulong Duan, Zhihong Liu, Guanglei Cui, and Liquan Chen. Progress in nitrile-based polymer electrolytes for high performance lithium ion batteries. *Journal of Material Chemistry A*. **4**, 10070-10083 (2016).
16. Huozhen Zhi, Lidan Xing, Xiongwen Zheng, Kang Xu, and Weishan Li. Understanding How Nitriles Stabilize Electrolyte/Electrode Interface at High Voltage. *J. Phys. Chem. Lett.* **8**, 6048–6052 (2017).
17. Xiaowei Li, Zhengxi Zhang, Sijian Li, Li Yang, Shin-ichi Hirano. Polymeric ionic liquid-plastic crystal composite electrolytes for lithium ion batteries. *Journal of Power Sources*. **307**, 678e683 (2016).
18. Hyo-Jeong Ha, Eun-Hye Kil, Yo Han Kwon, Je Young Kim, Chang Kee Lee and Sang-Young Lee. UV-curable semi-interpenetrating polymer network-integrated, highly bendable plastic crystal composite electrolytes for shape-conformable all-solid-state lithium ion batteries, *Energy Environ. Sci.* **5**, 6491 (2012).
19. Sim, L. H., Gan, S. N., Chan, C. H. & Yahya, R. ATR-FTIR studies on ion interaction of lithium perchlorate in polyacrylate/poly(ethylene oxide) blends. *Spectrochim. Acta Part A Mol. Biomol. Spectrosc.* **76**, 287–292 (2010).
20. Zhou, D.; He, Y.-B.; Liu, R.; Liu, M.; Du, H.; Li, B.; Cai, Q.; Yang, Q.-H.; Kang, F. In Situ Synthesis of a Hierarchical All-Solid-State Electrolyte Based on Nitrile Materials for High-Performance Lithium-Ion Batteries. *Adv. Energy Mater.* **5** (15), 1500353 (2015).

21. Huang, B., Wang, Z., Chen, L., Xue, R. & Wang, F. The mechanism of lithium ion transport in polyacrylonitrile-based polymer electrolytes. *Solid State Ionics* **91**, 279–284 (1996).
22. Shen, Y. *et al.* Solvation structure around the Li⁺ ion in succinonitrile–lithium salt plastic crystalline electrolytes. *Phys. Chem. Chem. Phys.* **18**, 14867–14873 (2016).
23. Hawthorne, H. M. & Sherwood, J. N. Lattice Defects in Plastic Organic Solids. *Trans. Faraday Soc* **66**, 1792–1798 (1969).
24. Lv, P.; Li, Y., Wu, Y.; Liu, G.; Liu, H.; Li, S., Tang, C.; Mei, J.; Li, Y. Robust Succinonitrile-Based Gel Polymer Electrolyte for Lithium-Ion Batteries Withstanding Mechanical Folding and High Temperature. *ACS Appl. Mater. Interfaces* **10** (30), 25384–25392 (2018).
25. Sai, R. *et al.* Role of polar side chains in Li⁺ coordination and transport properties of polyoxetane-based polymer electrolytes. *Phys. Chem. Chem. Phys.* **19**, 5185–5194 (2017).
26. Zhuang, G. V., Yang, H., Blizanac, B. & Ross, P. N. A Study of Electrochemical Reduction of Ethylene and Propylene Carbonate Electrolytes on Graphite Using ATR-FTIR Spectroscopy. *Electrochem. Solid-State Lett.* **8**, A441 (2005).
27. Reece, C. *An Introduction to Electrochemical Impedance Spectroscopy*, (Jefferson Labs, 2010).
28. Barsoukov, E. & Macdonald, J. R. (James R. *Impedance spectroscopy: theory, experiment, and applications*. (Wiley-Interscience, 2005).
29. A. AHMAD, K. B. M. I. & Z. O. Conductivity and Structural Studies of Plasticized Polyacrylonitrile (PAN) – Lithium Triflate Polymer Electrolyte Films. *Sains Malaysiana* **40**, 691–694 (2011).
30. Fu, X. *et al.* Inorganic and organic hybrid solid electrolytes for lithium-ion batteries. *CrystEngComm* **18**, 4236–4258 (2016).
31. Bhardwaj, S. K. *et al.* An overview of different strategies to introduce conductivity in metal–organic frameworks and miscellaneous applications thereof. *J. Mater. Chem. A* **6**, 14992–15009 (2018).
32. Dawood, S., Yarbrough, R., Davis, K. & Rathnayake, H. Self-assembly and optoelectronic properties of isorecticular MOF nanocrystals. *Synth. Met.* **252**, 107–112 (2019).

33. Kazyak, E. *et al.* Atomic layer deposition and first principles modeling of glassy $\text{Li}_3\text{BO}_3\text{--Li}_2\text{CO}_3$ electrolytes for solid-state Li metal batteries. *J. Mater. Chem. A* **6**, 19425–19437 (2018).
34. Han, X. *et al.* Negating interfacial impedance in garnet-based solid-state Li metal batteries. *Nat. Mater.* **16**, 572–579 (2017).
35. J.W. Lorimer, M.-T. Saugier-Cohtm Adad, C. L. Y. Alkali Metal and Ammonium Perchlorates Part I: Lithium and Sodium Perchlorates. *Int. UNION PURE Appl. Chem.* **61**, (1995).
36. Fujie, K., Ikeda, R., Otsubo, K., Yamada, T. & Kitagawa, H. Lithium Ion Diffusion in a Metal–Organic Framework Mediated by an Ionic Liquid. *Chem. Mater.* **27**, 7355–7361 (2015).
37. Meng, X., Wei, M.-J., Wang, H.-N., Zang, H.-Y. & Zhou, Z.-Y. Multifunctional luminescent Zn (ii)-based metal–organic framework for high proton-conductivity and detection of Cr^{3+} ions in the presence of mixed metal ions. *Dalt. Trans.* **47**, 1383–1387 (2018).
38. Merle, G., Wessling, M. & Nijmeijer, K. Anion exchange membranes for alkaline fuel cells: A review. *J. Memb. Sci.* **377**, 1–35 (2011).
39. Ameloot, R. *et al.* Ionic Conductivity in the Metal–Organic Framework UiO-66 by Dehydration and Insertion of Lithium *tert* -Butoxide. *Chem. - A Eur. J.* **19**, 5533–5536 (2013).
40. Chen, Z., Qin, Y. & Amine, K. Redox shuttles for safer lithium-ion batteries. *Electrochim. Acta* **54**, 5605–5613 (2009).
41. Seki, S. *et al.* Density, viscosity, ionic conductivity, and self-diffusion coefficient of organic liquid electrolytes: Part I. Propylene carbonate + Li, Na, Mg and Ca cation salts. *J. Electrochem. Soc.* **165**, A542–A546 (2018).
42. Southall, J. P. *et al.* Ionic conductivity and viscosity correlations in liquid electrolytes for incorporation into PVDF gel electrolytes. *Solid State Ionics* **85**, 51–60 (1996).
43. Nayak, J. N., Aralaguppi, M. I., Naidu, B. V. K. & Aminabhavi, T. M. Thermodynamic properties of water + tetrahydrofuran and water + 1,4-dioxane mixtures at (303.15, 313.15, and 323.15) K. *J. Chem. Eng. Data* **49**, 468–474 (2004).
44. Farhat, D., Lemordant, D., Jacquemin, J. & Ghamouss, F. Alternative Electrolytes for Li-Ion Batteries Using Glutaronitrile and 2-methylglutaronitrile with Lithium

- Bis(trifluoromethanesulfonyl) Imide. *J. Electrochem. Soc.* **166**, A3487–A3495 (2019).
45. Lee, J. Y., Yun, T. S., Santamarina, J. C. & Ruppel, C. Observations related to tetrahydrofuran and methane hydrates for laboratory studies of hydrate-bearing sediments. *Geochemistry, Geophys. Geosystems* **8**, (2007).
46. Nalwa, H. S. *Ferroelectric Polymers: Chemistry, Physics, and Applications*. (CRC Press, 1995).
47. Jarek, R. L., Miles, T. D., Trester, M. L., Denson, S. C. & Shin, S. K. Solvation of Li⁺ by acetone, THF, and diethyl ether in the Gas phase and the ion-molecule association mechanism. *J. Phys. Chem. A* **104**, 2230–2237 (2000).